

**COMPUTATIONAL STUDY OF SOLAR
FURNACE SYSTEM FOR THE APPLICATION IN
SOLAR PYROLYSIS OF MIXED PLASTIC
WASTE**

ONG JING XIAN

UNIVERSITI TUNKU ABDUL RAHMAN

**COMPUTATIONAL STUDY OF SOLAR FURNACE SYSTEM FOR
THE APPLICATION IN SOLAR PYROLYSIS OF MIXED PLASTIC
WASTE**

ONG JING XIAN

**A project report submitted in partial fulfilment of the
requirements for the award of Bachelor of Science (Honours) Physics**

**Lee Kong Chian Faculty of Engineering and Science
Universiti Tunku Abdul Rahman**

May 2023

DECLARATION

I hereby declare that this project report is based on my original work except for citations and quotations which have been duly acknowledged. I also declare that it has not been previously and concurrently submitted for any other degree or award at UTAR or other institutions.

Signature : Ong

Name : Ong Jing Xian

ID No. : 1600831

Date : 19/5/2023

APPROVAL FOR SUBMISSION

I certify that this project report entitled “**COMPUTATIONAL STUDY OF SOLAR FURNACE SYSTEM FOR THE APPLICATION IN SOLAR PYROLYSIS OF MIXED PLASTIC WASTE**” was prepared by **ONG JING XIAN** has met the required standard for submission in partial fulfilment of the requirements for the award of Bachelor of Science (Honours) Physics at Universiti Tunku Abdul Rahman.

Approved by,

Signature : _____

Supervisor : _____

Date : _____

Signature : _____

Co-Supervisor : _____

Date : _____

The copyright of this report belongs to the author under the terms of the copyright Act 1987 as qualified by Intellectual Property Policy of Universiti Tunku Abdul Rahman. Due acknowledgement shall always be made of the use of any material contained in, or derived from, this report.

© 2023, Ong Jing Xian. All right reserved.

ACKNOWLEDGEMENTS

I would like to express my gratitude to my research supervisor, Prof. Dr. Chong Kok Keong for his invaluable advice, guidance and his enormous patience throughout the development of the research.

ABSTRACT

While several studies on various aspects of the solar furnace system have been conducted, optimization of the simulation has not received much attention. The purpose of this study is to find the optimal resolutions that produce reasonably accurate results. Solar flux distribution maps were obtained using a simulation software, in which the detailed methodology of ray-tracing algorithm is presented. The optimal resolutions found that take into account value and geometrical profile of flux distribution are $k_1 = 46 \times 10^{-3}$ and $k_2 = 15 \times 10^{-3}$. In addition, the simulation results are verified and the feasibility of solar furnace for application in solar pyrolysis of mixed plastic waste is demonstrated.

TABLE OF CONTENTS

DECLARATION	i
APPROVAL FOR SUBMISSION	ii
ACKNOWLEDGEMENTS	iv
ABSTRACT	v
TABLE OF CONTENTS	vi
LIST OF TABLES	viii
LIST OF FIGURES	ix
LIST OF SYMBOLS / ABBREVIATIONS	xi

CHAPTER

1	INTRODUCTION	1
	1.1 General Introduction	1
	1.2 Problem Statement	1
	1.3 Aim and Objectives	2
2	LITERATURE REVIEW	3
	2.1 Introduction	3
	2.2 Literature Review	3
	2.3 Conclusion	8
3	METHODOLOGY AND WORK PLAN	9
	3.1 Introduction	9
	3.2 Requirement/ Specification/ Standards	10
	3.3 Methodology	10
	3.3.1 Heliostat	11
	3.3.2 Modelling of Numerical Simulation	12
	3.3.3 Resolution	18
4	RESULTS AND DISCUSSION	20
	4.1 Introduction	20
	4.2 Optimization	21
	4.2.1 Importance of Optimization	22

4.2.2	Optimization Techniques	23
4.2.3	Comparison with Highest Resolution	28
4.3	Verification of Simulation Results	29
4.3.1	Temperature Distribution Map	31
4.3.2	Comparison between Experimental and Simulation Results	32
4.4	Solar Pyrolysis of Mixed Plastic Waste	34
4.4.1	Feasibility of Solar Furnace	34
5	CONCLUSIONS AND RECOMMENDATIONS	39
5.1	Conclusions	39
5.2	Recommendations for Future Work	39
	REFERENCES	40

LIST OF TABLES

Table 3.1:	Specifications of the Simulation.	10
Table 4.1:	Top of Flux Distribution for Increasing k_1 for Fixed k_2 .	26
Table 4.2:	Top of Flux Distribution for Increasing k_2 for Fixed k_1 .	27
Table 4.3:	Comparison between Optimal Resolution, Highest k_1 and Lowest Maximum Solar Concentration, and Highest k_2 and Largest Number of Rays.	28
Table 4.4:	Specifications for the Simulation of Solar Furnace Described in an Article by Lim and Li.	30
Table 4.5a:	Flux Distribution, Temperature Map and Solar Irradiance Data at Yinchuan, Ningxia, China on 21 June 2021 (Summer Solstice).	36
Table 4.5b:	Flux Distribution, Temperature Map and Solar Irradiance Data at Yinchuan, Ningxia, China on 22 December 2022 (Winter Solstice).	37
Table 4.5c:	Flux Distribution, Temperature Map and Solar Irradiance Data at Yinchuan, Ningxia, China on 20 March 2022 (Vernal Equinox).	38

LIST OF FIGURES

Figure 2.1:	Rotation and Elevation Movement of New Heliostat Design.	4
Figure 2.2:	Side View of 5×5 Mirror Heliostat.	4
Figure 2.3:	Intensity Concentration Profile of Solar Furnace.	6
Figure 2.4:	Schematic Diagram of Flux Mapping System.	7
Figure 2.5:	Setup Used for Indirect Heating.	8
Figure 3.1:	User Interface of Solar Furnace Using Non-Imaging Focusing Heliostat Software.	9
Figure 3.2:	Schematic Diagram to Show Configuration of Solar Furnace System and Cone Ray.	13
Figure 3.3:	Slope Error.	13
Figure 4.1:	3D Plot of Solar Flux Distribution.	20
Figure 4.2:	2D Plot of Solar Flux Distribution.	21
Figure 4.3:	Graph of Computation Time Versus Total Number of Rays Traced.	22
Figure 4.4:	Graph of Deviation of Maximum Solar Concentration Versus Simulation Time.	23
Figure 4.5:	Graph of Maximum Solar Concentration Versus k_1 for Fixed k_2 .	24
Figure 4.6:	Graph of Maximum Solar Concentration Versus k_2 for Fixed k_1 .	24
Figure 4.7:	Steel Plate Melted by a Solar Furnace.	29
Figure 4.8:	Top View of Solar Flux Distribution of Steel Plate.	31
Figure 4.9:	Temperature Distribution Map of Steel Plate.	32
Figure 4.10:	Comparison of Melted Steel Plate and Temperature Distribution Map.	33
Figure 4.11:	Melting Contour Overlaid on Top of the Steel Plate.	33

- Figure 4.12: Variation of Incidence Angle of Heliostat Operating at Yinchuan, Ningxia, China. 34
- Figure 4.13: Variation of Rotation Angle of Heliostat Operating at Yinchuan, Ningxia, China. 35

LIST OF SYMBOLS / ABBREVIATIONS

θ	elevation angle, °
ρ	spinning angle, °
δ	declination angle, °
Φ	latitude angle, °
ω	hour angle, °
φ	facing angle, °
λ	target angle, °
σ	line-tilted angle for mirrors located in the same row, °
γ	line-tilted angle for mirrors located in the same column, °
$\Delta\sigma$	preset angle for σ , °
$\Delta\gamma$	preset angle for γ , °
θ_{preset}	preset incident angle, °
α	half angle of cone ray, °
θ_{ij}	local incident angle relative to the corresponding i,j -mirror, °
δ	slope error
χ	circumsolar ratio
p	total number of sub-rays per cone ray
H_{Cx}	perpendicular distance between the centre of heliostat and the central line of the row where the concerned mirror is located, cm
H_{Cy}	perpendicular distance between the centre of heliostat and the central line of the column where the concerned mirror is located, cm
L	primary focal distance of the heliostat or the distance from the heliostat to the vertex of secondary concentrator, cm
f_s	focal length of secondary concentrator, cm
L_p	displacement of target plane from focal plane of secondary concentrator, cm
C	solar concentration ratio, suns
C_{max}	maximum solar concentration ratio, suns

n_{MR}	number of reflective points per row or column of the mirror
n_{SD}	number of sub-rays along the radial direction of the cone ray from the centre to the edge of the solar disc
n_{TR}	number of pixels per row or column of the target plane
w	mirror size, cm
R_{SD}	radius of cone ray at target plane, cm
T_s	target size, cm
r_{MR}	resolution of mirror, pixel/cm ²
r_{SD}	resolution of cone ray, pixel/cm ²
r_{TR}	resolution of target plane, pixel/cm ²
k_1	mirror resolution factor
k_2	cone ray resolution factor

CHAPTER 1

INTRODUCTION

1.1 General Introduction

A solar furnace is a system that produces high temperatures by concentrating sunlight. It consists of a primary heliostat and a secondary concentrator. A heliostat consists of an array of mirrors on a frame that tracks and focuses sun rays via reflection, whereas a secondary concentrator can be either a parabolic or spherical reflector to further focus the rays. At the focal point, temperatures may reach as high as 3500 °C. The heat energy produced can be used in various applications such as pyrolysis and solar thermal power.

With recent advancements in the processing power of computers, it is now feasible to model and simulate complicated systems that do not have analytical solutions. One such system is the solar furnace. Comprehensive modelling of the mirrors and light rays paired with a ray-tracing technique is required to obtain a realistic solar flux distribution map produced on the target. In this report, a methodology for modelling the solar furnace is presented. Then, techniques to optimize the simulation time and resolutions for obtaining reasonably accurate results are suggested.

Simulation results can be verified through comparisons with experimental results. The flux distribution map obtained from simulation can be converted into temperature distribution map, which can then be compared with an object melted by solar furnace. The criteria that are used to judge the accuracy of the simulation result are the size and shape of the melting spot.

In a previous study, the best temperature for the pyrolysis of plastic waste in terms of conversion and product quality was determined to be 500 °C or 773 K. To show that the solar furnace is suitable for application in solar pyrolysis, simulations for various operating conditions at Yinchuan, Ningxia, China has been performed.

1.2 Problem Statement

As demonstrated by several published papers, the flux distribution of a solar furnace which consists of a heliostat and a secondary concentrator can be

obtained via a digital simulation approach. However, it is time consuming. Depending on the resolutions used and the processing power of the computer, it can take up to a few days to complete for just one operating condition. If the solar power tower which consists of multiple heliostats and multiple operating conditions are considered, the time needed will add up quickly. While attempts to optimize the system have previously been made, in this report, resolution is redefined, and new optimal resolutions are found.

With the increasing global population, rapid urbanization, and lifestyle changes, plastic waste production is rising at an alarming rate. This issue is further aggravated by the brief lifespan of plastic. As of right now, around 300 million tonnes of plastic are produced globally each year. Most plastics, such as polyethylene, polypropylene, polystyrene, poly(vinyl chloride) and poly(ethylene terephthalate) are non-biodegradable. Different methods of recycling plastic waste exist, however, in the majority of developing countries, open or landfill disposal is a prevalent method of managing plastic waste. The disposal of non-biodegradable plastic waste in landfills could provide a habitat for pests such as insects and rodents that may carry diseases. Furthermore, the available space for landfills is also diminishing (Miandad, et al., 2019). Pyrolysis, which is the thermal decomposition of materials at high temperatures, seems to be a promising alternative solution.

1.3 Aim and Objectives

The aim of this report is to understand various aspects of the solar furnace system. To achieve the aim, the objectives must be defined. The objectives are:

- (i) To study the primary tracking of heliostat frame/ master mirror and secondary tracking of slave mirrors.
- (ii) To understand the digital simulation approach to obtain flux distribution of the solar image formed on the target plane.
- (iii) To find the optimal resolutions for reasonably accurate results.
- (iv) To verify the simulation result through comparisons with experimental result.
- (v) To determine the feasibility of solar furnace for application in solar pyrolysis.

CHAPTER 2

LITERATURE REVIEW

2.1 Introduction

Interest in the modern solar furnace began in the 1940s. Built in France in 1949, the Mont-Louis solar furnace (Trombe, 1957) was believed to be the world's first solar furnace. It was an experimental solar furnace that led to the construction of the Odeillo solar furnace (Trombe and Le Phat Vinh, 1973) in 1962. Other famous solar furnaces that were built in that period include the Arizona State College solar furnace (Kevane, 1957) in the USA and the solar furnace of Government Industrial Research Institute (Hisada, et al., 1957) in Japan. More recently, a spinning-elevation tracking heliostat based on non-imaging optics has been proposed (Chen, et al., 2001). Furthermore, with major advancements in computing power, digital simulation techniques have been employed to study the optical behavior of the solar furnace (Lim and Li, 2009). In this chapter, the developments of solar furnace leading up to simulations and their applications are recapped.

2.2 Literature Review

Chen, et al. (2001) proposed a new design to the conventional heliostat. In this design, the mirrors are arranged in a plane in rows and columns. Tracking is described in two parts: primary tracking of the heliostat frame/ master mirror and secondary tracking of the slave mirrors. The movement of primary tracking is described by two independent components, namely, rotation movement that ensures the sun and target are in the same plane of reflection, and elevation movement that ensures the normal of the heliostat frame/ master mirror bisects the angle formed by sun and target (Figure 2.1). Secondary tracking focuses the reflected rays on the target by rotating the slave mirrors through an angle. In this mode, slave mirrors in the same row or column will have the same movement (Figure 2.2). The benefit compared to the conventional azimuth-elevation tracking heliostat is that the number of slave mirror controlling devices required is significantly reduced. For example, if the conventional heliostat consists of M rows and N columns of element mirrors, $2 \times M \times N$ controlling devices have

to be used as each mirror requires 2 degrees of freedom. With the new design, the elevation axis is maintained perpendicular to the plane containing sun, normal and target through rotation movement. Slave mirrors in the same row or column can share the same controlling device, reducing the number required to $M + N$.

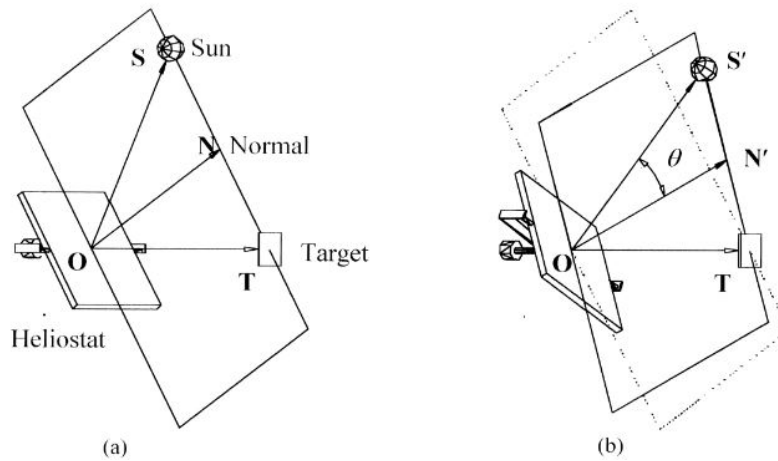


Figure 2.1: Rotation and Elevation Movement of New Heliostat Design (Chen, et al., 2001).

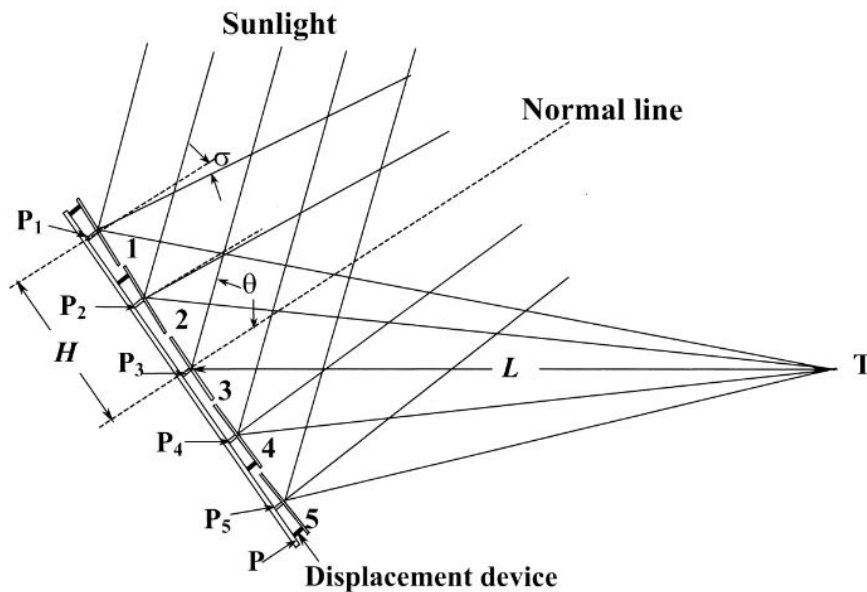


Figure 2.2: Side View of 5×5 Mirror Heliostat (Chen, et al., 2001).

According to Lim and Li (2009), a fixed target solar furnace usually consists of a heliostat as the primary stage and a concentrator (e.g., parabolic and spherical dish) as the secondary stage. As the analytical study of this system is complicated, a digital simulation approach to study the flux distribution of solar furnace was proposed. The approach was to use a ray-tracing method with intensity calibration. In this method, the heliostat mirrors are subdivided into smaller elements, which each are then associated with a position vector to represent its spatial coordinates and unit vector to represent its normal. Matrices are used to describe the transformations of these vectors during sun tracking. After that, light rays are impinged onto each mirror element, and the rays are traced using straight lines to the secondary concentrator and then to the target plane. If solar disc effect is considered, the reflected rays from mirror elements are dispersed uniformly into N sub-rays such that it forms a light cone which subtends to solar disc half-angle of 4.65 mrad. The author notes that the effect of the sun's atmosphere which gives the disc a limb darkening is ignored by this pillbox sunshape. The target plane is similarly subdivided into smaller pixels, in which its flux intensity can be recorded by summing up the calibrated intensity of the sub-rays that hit it. Figure 2.3 shows the intensity concentration profile of a solar furnace with settings: target position 21 cm from vertex of secondary concentrator, incident angle of 14.05° , canting angle of 36° , 5×5 m heliostat with 11×11 spherical mirrors, spherical concentrator focal length of 23 cm.

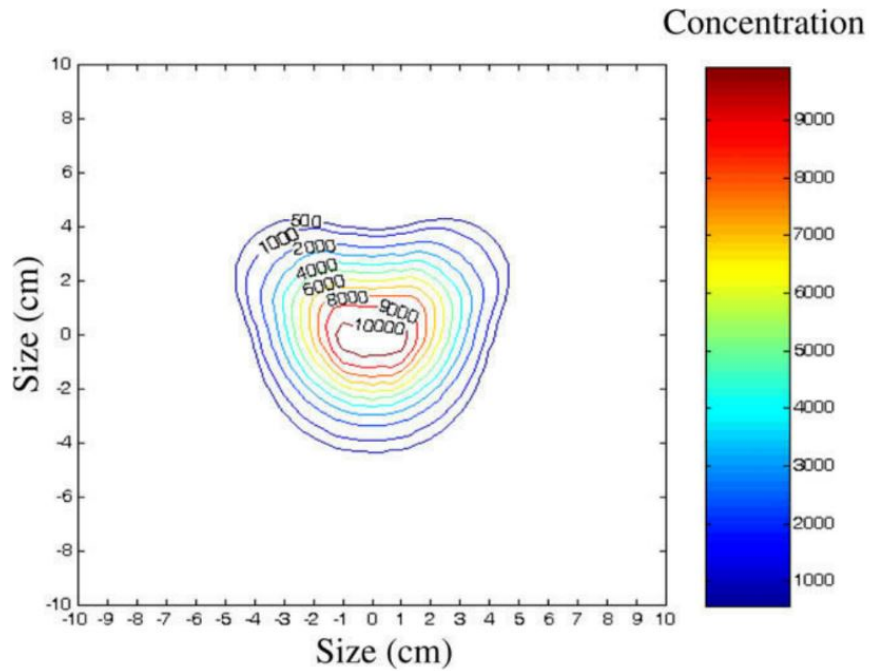


Figure 2.3: Intensity Concentration Profile of Solar Furnace (Lim and Li, 2009).

Lee, et al. (2014) evaluated the performance of a solar furnace at Korea Institute of Energy Research (KIER) by measuring the flux with the flux mapping method and by comparing with results using a ray-tracing method. A diffuse target, heat flux gauge, a charge-coupled device (CCD) camera and a computer are essential components of the flux mapping system (Figure 2.4). The CCD camera captures the image formed on the diffuse target. By converting the pixel gray level to a number, a two-dimensional matrix of the brightness can be obtained. This matrix is proportional to the flux distribution because brightness and flux are linearly proportional. It can then be calibrated using a reference measurement with the heat flux gauge. After adjusting the parabolic concentrator facets, the solar furnace was able to achieve 40 kW and 90% of it was within 166 mm² aperture. The maximum solar concentration ratio was 5050 suns. By comparing the results from measurements and modelling, the slope error was determined to be approximately 2.2 mrad.

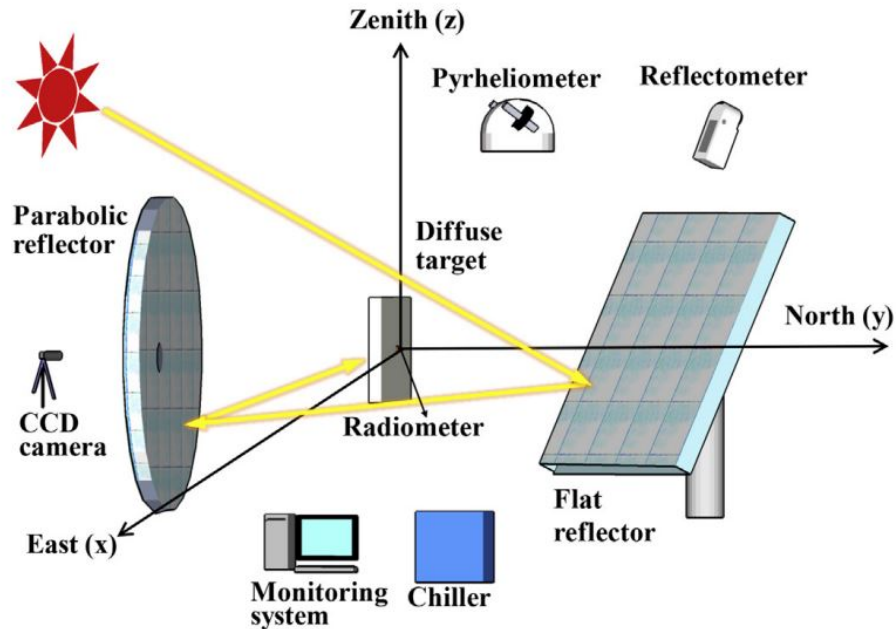


Figure 2.4: Schematic Diagram of Flux Mapping System (Lee, et al., 2014).

Solar furnaces are infrequently used today for material processing. Not only are such facilities costly to operate and maintain, but it is also challenging to regulate temperature in such a way that the process is practical in large-scale commercial plants. Due to the Gaussian distribution of the solar flux distribution in the focal area, it is very challenging to guarantee a uniform temperature distribution over the material when it is directly subjected to concentrated solar radiation. Oliveira, et al. (2016) suggests that the indirect heating of solar radiation could enable thermal processing of materials under controlled and consistent heating. This requires the selection of suitable heat absorber materials that can absorb and transfer heat effectively and affordably. In the study, graphite was chosen as the receiver material due to its resistance to high temperature, good thermal conductivity and high emissivity. Figure 2.5 depicts an indirect heating setup. In another study (Li, et al., 2015), other materials were also used as receivers, namely stainless steel AISI 310 and molybdenum disilicide (MoSi_2). MoSi_2 is an intermetallic compound that has several qualities that make it an excellent choice for use as a high temperature heating element. It has an excellent resistance to oxidation, a moderate density (6.24 g/cm^3), and an extremely high melting point of 2303 K.

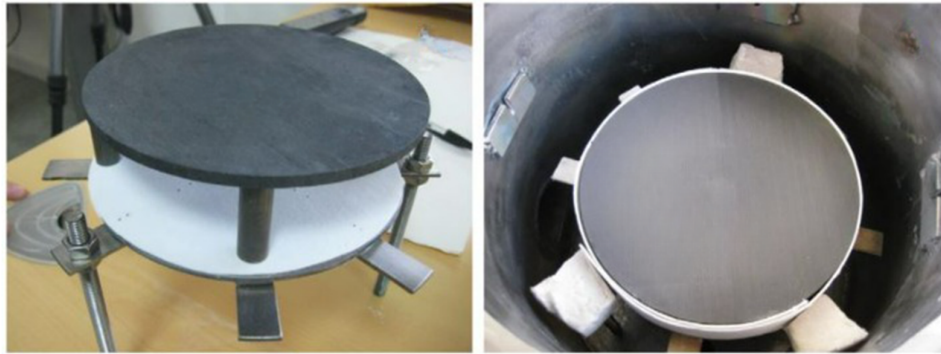


Figure 2.5: Setup Used for Indirect Heating (Oliveira, et al., 2016).

2.3 Conclusion

The purpose of this review is to help the reader to keep up with the developments of the solar furnace system. The examples reviewed demonstrate enormous potential of using solar furnace for high temperature applications, despite certain limitations that prevent a uniform distribution of temperature. Although previous research on the solar furnace has been very comprehensive, which includes its designs, simulations and applications, there has not been much focus on the optimization of the simulation. Optimizing the resolution in terms of simulation time and result accuracy can play an important role in the efficiency and even feasibility of the simulations.

CHAPTER 3

METHODOLOGY AND WORK PLAN

3.1 Introduction

The flux distribution maps were obtained via a new Solar Furnace software using Non-Imaging Focusing Heliostat. Figure 3.1 shows the user interface of the software. This simulation software was developed using Microsoft Visual C++ by my project supervisor. After entering in the parameter values and selecting secondary concentrator type, the simulation is performed and a .dat file containing a 201 x 201 matrix is created. This file is then opened in MATLAB, which is able to produce the necessary plots. The simulation is repeated with various combinations of resolutions. Microsoft Excel is also used for storing data, performing calculations and plotting graphs.

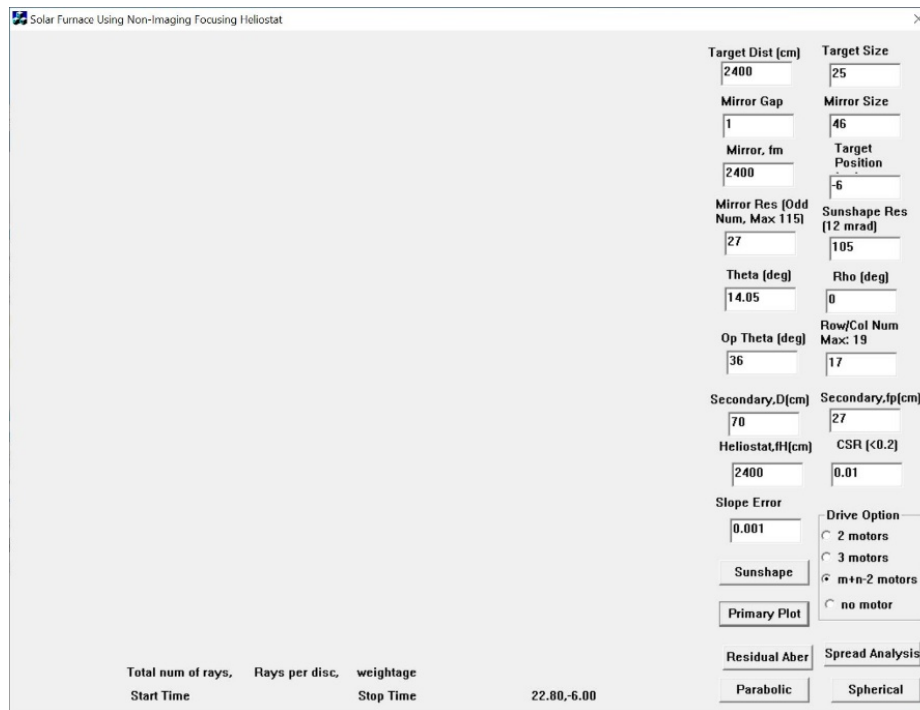


Figure 3.1: User Interface of Solar Furnace Using Non-Imaging Focusing Heliostat Software.

3.2 Requirement/ Specification/ Standards

The specifications used for the case study are listed in Table 3.1.

Table 3.1: Specifications of the Simulation.

Parameter	Value
Target distance	2400 cm
Target size	25 cm
Mirror gap	1 cm
Mirror size	46 cm
Mirror focal length	2400 cm
Target position	-6 cm
Pixels per mirror	Variable
Pixels per solar disc	Variable
Incident angle	14.05°
Spinning angle	0
Operational angle	36°
Number of row and column	17
Secondary concentrator diameter	70 cm
Secondary concentrator focal length	27 cm
Heliostat focal length	2400 cm
CSR	0.01
Slope error	0.001
Motor	M+N-2 motor
Secondary concentrator type	Parabolic

The specifications of the computer used for the simulation: 12th Gen Intel® Core™ i5-12400, 2.50 GHz, 8.00 GB RAM.

3.3 Methodology

To analyse the flux distribution, a coordinate transformation and ray-tracing method are employed to model the solar furnace and heliostat. The objective of coordinate transformation is to describe the movement of heliostat frame and mirror, and ray-tracing method is to find the final hitting point of reflected

sunray on the target plane by tracking the rays from mirror to concentrator to target plane.

3.3.1 Heliostat

The formulas for heliostat are briefly presented in this report (Chen, et al., 2001; Chong, 2010). A heliostat performs two functions concurrently, which is to track the sun and focus the reflected rays. For the heliostat to perform sun-tracking, the spinning and elevation angles of the heliostat frame:

$$\theta = \frac{\pi}{4} - \frac{1}{2} \sin^{-1} \left(\begin{array}{l} \cos \delta \cos \omega (\sin \lambda \cos \Phi - \cos \lambda \cos \varphi \sin \Phi) \\ - \cos \delta \sin \omega \cos \lambda \sin \varphi \\ + \sin \delta (\cos \lambda \cos \varphi \cos \Phi + \sin \Phi \sin \lambda) \end{array} \right) \quad (3.1)$$

$$\cos \rho = \frac{1}{\cos(\pi/2 - 2\theta)} \left\{ \begin{array}{l} \cos \delta \cos \omega (\cos \lambda \cos \Phi + \sin \lambda \cos \varphi \sin \Phi) \\ + \sin \lambda \sin \varphi \cos \delta \sin \omega \\ + \sin \delta (\cos \lambda \sin \Phi - \sin \lambda \cos \varphi \cos \Phi) \end{array} \right\} \quad (3.2)$$

for $\cos \rho > 0$,

$$\rho_+ = \sin^{-1} \left\{ \frac{-\cos \delta \cos \omega \sin \varphi \sin \Phi + \cos \delta \sin \omega \cos \varphi + \sin \delta \sin \varphi \cos \Phi}{\cos(\pi/2 - 2\theta)} \right\} \quad (3.3a)$$

for $\cos \rho < 0$,

$$\rho_- = \pi - \sin^{-1} \left\{ \frac{-\cos \delta \cos \omega \sin \varphi \sin \Phi + \cos \delta \sin \omega \cos \varphi + \sin \delta \sin \varphi \cos \Phi}{\cos(\pi/2 - 2\theta)} \right\} \quad (3.3b)$$

where θ the elevation angle, ρ is the spinning angle, δ is the declination angle, Φ is the latitude angle, ω is the hour angle, φ is the facing angle and λ is the target angle.

For the slave mirrors to perform ray focusing, the line-tilted angle for mirrors located in the same row and line-tilted angle for mirrors located in the same column:

$$\sigma = \frac{1}{2} \tan^{-1} \left(\frac{H_{Cx} \cos \theta}{H_{Cx} \sin \theta + L} \right) \quad (3.4)$$

$$\gamma = \frac{1}{2} \tan^{-1} \left(\frac{H_{Cy}}{L \cos \theta} \right) \quad (3.5)$$

where σ is the line-tilted angle for mirrors located in the same row, γ is the line-tilted angle for mirrors located in the same column, H_{Cx} is the perpendicular distance between the centre of heliostat and the central line of the row where the

concerned mirror is located, H_{cy} is the perpendicular distance between the centre of heliostat and the central line of the column where the concerned mirror is located and L is the primary focal distance of the heliostat or the distance from the heliostat to the vertex of secondary concentrator.

To model pre-setting element mirrors, additional line-tilted angles $\Delta\sigma$ and $\Delta\gamma$, which are constants in the function of preset incident angle, θ_{preset} , are added to σ and γ to form $(\sigma + \Delta\sigma)$ and $(\gamma + \Delta\gamma)$.

3.3.2 Modelling of Numerical Simulation

In the development of ray-tracing algorithm, three assumptions have been made. Firstly, as illustrated in Figure 3.2, the mirror is subdivided into smaller elements called reflective points, each with its own coordinate and unit normal vector.

Secondly, slope error is introduced to consider the imperfections of the mirrors due to manufacturing errors or mechanical deformation. It is defined as the random error deviation from the ideal surface normal, which distorts the reflected ray. Figure 3.3 illustrates how slope error causes deviation of reflected ray. The deviation from the normal (Wong, Chong and Tan, 2015):

$$\theta_r = \sqrt{(-2\delta^2) \ln(1 - r_\theta)} \quad 0 \leq r_\theta \leq 1 \quad (3.6)$$

$$\varphi = 2\pi r_\varphi \quad 0 \leq r_\varphi \leq 1 \quad (3.7)$$

where r_θ and r_φ are random numbers and δ is the standard deviation of slope error (also known in short as slope error).

Thirdly, the sunshape is modelled as a limb-darkened solar disc with circumsolar radiation. As illustrated in Figure 3.2, each reflected ray from the heliostat mirror is treated as a cone ray that spreads the reflected ray into p sub-rays. Each sub-ray occupies an equal cross-sectional area with radiance energy (Buie, Monger and Dey, 2003):

$$\hat{L}(\alpha_i) = \begin{cases} \frac{\cos(0.326\alpha_i)}{\cos(0.308\alpha_i)} & 0 \leq \alpha_i \leq \alpha_{sun} \\ e^{\kappa\alpha_i^\gamma} & \alpha_{sun} \leq \alpha_i \leq \alpha_{aur} \end{cases} \quad (3.8)$$

where $\kappa = 0.9 \ln(13.5\chi)\chi^{-0.3}$, $\gamma = 2.2 \ln(0.52\chi)\chi^{0.43} - 0.1$, χ is the circumsolar ratio (CSR), α_i is the radial displacement about the solar vector, α_{sun} is the solar disc half angle of 4.65 mrad, α_{aur} is the angular extent of the aureole of 12 mrad, $i = 1, 2, 3, \dots, p$ and p is the total number of sub-rays within cone ray.

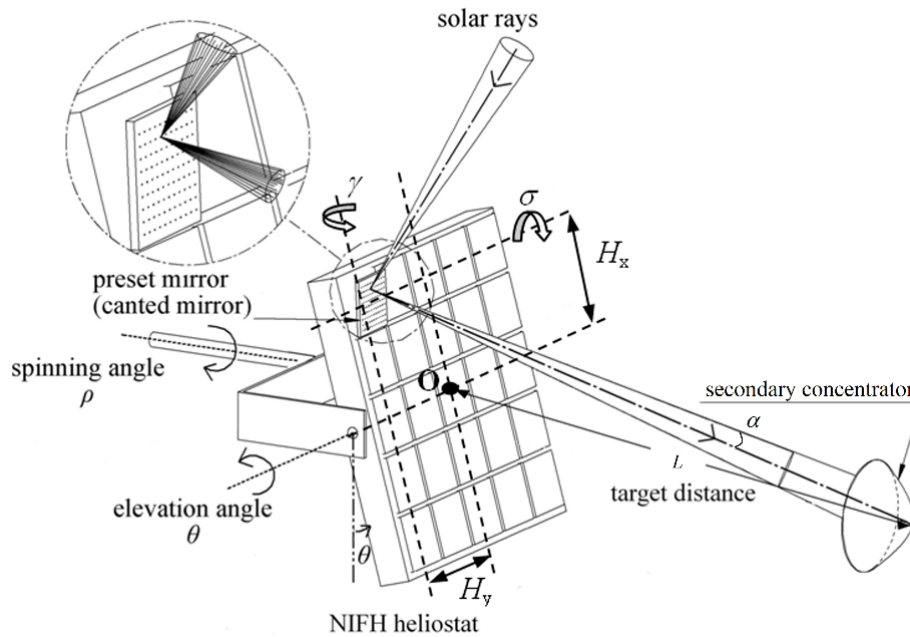


Figure 3.2: Schematic Diagram to Show Configuration of Solar Furnace System and Cone Ray.

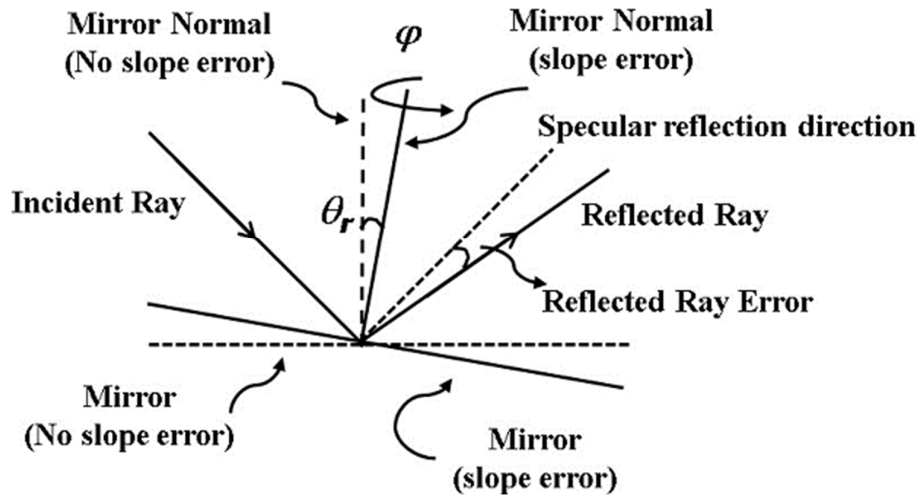


Figure 3.3: Slope Error (Wong, Chong and Tan, 2015).

The Cartesian coordinate system is defined by:

- (i) The centre of the heliostat is at the origin O (0, 0, 0).
- (ii) Z axis points towards the target.
- (iii) X axis and Y axis are parallel with vertical and horizontal directions of heliostat frame at the initial orientation respectively.

The reflective point on heliostat mirror is called primary reflective point, while the reflective point on secondary concentrator is called secondary reflective point. The initial coordinate of a primary reflective point is represented by $H_{ijkl} = (H_x, H_y, H_z)_{ijkl}$, where the subscripts are the counters: i and j represent row and column of the mirror respectively, k and l represent row and column of the reflective point respectively. Tracking changes H_{ijkl} to new coordinate $H'_{ijkl} = (H'_x, H'_y, H'_z)_{ijkl}$. A 4 x 4 transformation matrix is adopted to describe the transformation (Lu and Sung, 2013):

$$H'_{ijkl} = M_{ij}H_{ijkl} \quad (3.9)$$

$$\text{where } H'_{ijkl} = \begin{bmatrix} H'_x \\ H'_y \\ H'_z \\ 1 \end{bmatrix}_{ijkl}, H_{ijkl} = \begin{bmatrix} H_x \\ H_y \\ H_z \\ 1 \end{bmatrix}_{ijkl},$$

$$M_{ij} = [\rho][\theta][T_2][\gamma + \Delta\gamma][\sigma + \Delta\sigma][T_1], \quad (3.10)$$

$$[\rho] = \begin{bmatrix} \cos \rho & \sin \rho & 0 & 0 \\ -\sin \rho & \cos \rho & 0 & 0 \\ 0 & 0 & 1 & 0 \\ 0 & 0 & 0 & 1 \end{bmatrix}, [\theta] = \begin{bmatrix} \cos \theta & 0 & \sin \theta & 0 \\ 0 & 1 & 0 & 0 \\ -\sin \theta & 0 & \cos \theta & 0 \\ 0 & 0 & 0 & 1 \end{bmatrix},$$

$$[T_1] = \begin{bmatrix} 1 & 0 & 0 & -H_x \\ 0 & 1 & 0 & -H_y \\ 0 & 0 & 1 & -H_z \\ 0 & 0 & 0 & 1 \end{bmatrix}, [T_2] = \begin{bmatrix} 1 & 0 & 0 & H_x \\ 0 & 1 & 0 & H_y \\ 0 & 0 & 1 & H_z \\ 0 & 0 & 0 & 1 \end{bmatrix},$$

$$[\gamma + \Delta\gamma] = \begin{bmatrix} 1 & 0 & 0 & 0 \\ 0 & \cos(\gamma + \Delta\gamma) & -\sin(\gamma + \Delta\gamma) & 0 \\ 0 & \sin(\gamma + \Delta\gamma) & \cos(\gamma + \Delta\gamma) & 0 \\ 0 & 0 & 0 & 1 \end{bmatrix},$$

$$[\sigma + \Delta\sigma] = \begin{bmatrix} \cos(\sigma + \Delta\sigma) & 0 & -\sin(\sigma + \Delta\sigma) & 0 \\ 0 & 1 & 0 & 0 \\ \sin(\sigma + \Delta\sigma) & 0 & \cos(\sigma + \Delta\sigma) & 0 \\ 0 & 0 & 0 & 1 \end{bmatrix}.$$

On the other hand, the initial normal of the reflective points can be described by unit normal vector $\widehat{N}_{ijkl} = N_x\hat{x} + N_y\hat{y} + N_z\hat{z}$.

$$\mathbf{N}_{ijkl} = \begin{bmatrix} N_x \\ N_y \\ N_z \\ 1 \end{bmatrix}_{ijkl} = \frac{1}{2L} \begin{bmatrix} H_{cx} - H_x \\ H_{cy} - H_y \\ 2L - H_z \\ 1 \end{bmatrix}_{ijkl} \quad (3.11)$$

Tracking changes \widehat{N}_{ijkl} to new unit normal vector $\widehat{N}'_{ijkl} = N'_x\hat{x} + N'_y\hat{y} + N'_z\hat{z}$. The transformation that models tracking and slope error is described by:

$$\mathbf{N}'_{ijkl} = M'_{ijkl}\mathbf{N}_{ijkl} \quad (3.12)$$

$$\text{where } \mathbf{N}'_{ijkl} = \begin{bmatrix} N'_x \\ N'_y \\ N'_z \\ 1 \end{bmatrix}_{ijkl}, \quad \mathbf{N}_{ijkl} = \begin{bmatrix} N_x \\ N_y \\ N_z \\ 1 \end{bmatrix}_{ijkl},$$

$$M'_{ijkl} = [\rho][\theta][\gamma + \Delta\gamma][\sigma + \Delta\sigma][\theta_r][\varphi], \quad (3.13)$$

$$[\varphi] = \begin{bmatrix} \cos \varphi & -\sin \varphi & 0 & 0 \\ \sin \varphi & \cos \varphi & 0 & 0 \\ 0 & 0 & 1 & 0 \\ 0 & 0 & 0 & 1 \end{bmatrix}_{ijkl}, \quad [\theta_r] = \begin{bmatrix} 1 & 0 & 0 & 0 \\ 0 & \cos \theta_r & -\sin \theta_r & 0 \\ 0 & \sin \theta_r & \cos \theta_r & 0 \\ 0 & 0 & 0 & 1 \end{bmatrix}_{ijkl}.$$

Furthermore, the unit vector of incident sunray is defined as $\hat{I} = I_x\hat{x} + I_y\hat{y} + I_z\hat{z}$, which is described by:

$$\mathbf{I} = \begin{bmatrix} I_x \\ I_y \\ I_z \\ 1 \end{bmatrix} = \begin{bmatrix} \cos(0.5\pi - 2\theta) \cos \rho \\ -\cos(0.5\pi - 2\theta) \sin \rho \\ \sin(0.5\pi - 2\theta) \\ 1 \end{bmatrix} \quad (3.14)$$

Now that both unit vectors of incident sunray and normal of reflective points are obtained, the unit vector of primary reflected ray, $\hat{R}_{ijkl} = R_x \hat{x} + R_y \hat{y} + R_z \hat{z}$, can be obtained as:

$$\mathbf{R}_{ijkl} = \begin{bmatrix} R_x \\ R_y \\ R_z \\ 1 \end{bmatrix}_{ijkl} = \begin{bmatrix} 2(I_x N'_x + I_y N'_y + I_z N'_z) N'_x - I_x \\ 2(I_x N'_x + I_y N'_y + I_z N'_z) N'_y - I_y \\ 2(I_x N'_x + I_y N'_y + I_z N'_z) N'_z - I_z \\ 1 \end{bmatrix}_{ijkl} \quad (3.15)$$

Each primary reflected ray is treated as a cone ray that spreads the reflected ray into p sub-rays, each sub-ray is then denoted as $\hat{R}_{ijkl,s} = R_{sx} \hat{x} + R_{sy} \hat{y} + R_{sz} \hat{z}$, where $s = 1, 2, 3, \dots, p$. Given unit vector of sub-ray and coordinate of primary reflective point, the line equation can then be constructed:

$$\frac{P_{sx} - H'_x}{R_{sx}} = \frac{P_{sy} - H'_y}{R_{sy}} = \frac{P_{sz} - H'_z}{R_{sz}} \quad (3.16)$$

where $P_{ijkl,s} = (P_{sx}, P_{sy}, P_{sz})_{ijkl,s}$ is the coordinate of secondary reflective point of the secondary concentrator, which can be parabolic or spherical with its vertex at $(0, 0, L)$ and focal length f_s . The diameter (aperture) is also considered.

The surface equation of parabolic concentrator:

$$S = P_{sx}^2 + P_{sy}^2 + 4f_s(P_{sz} - L) \quad (3.17a)$$

The surface equation of spherical concentrator:

$$S = P_{sx}^2 + P_{sy}^2 + (P_{sz} - L + 2f_s)^2 - (2f_s)^2 \quad (3.17b)$$

To obtain coordinate of secondary reflective point $P_{ijkl,s}$, the value of equation 3.17 is set to zero and solved simultaneously with equation 3.16. To obtain unit normal vector $N''_{ijkl,s} = N''_{sx} \hat{x} + N''_{sy} \hat{y} + N''_{sz} \hat{z}$ of the secondary concentrator:

$$\mathbf{N}''_{ijkl,s} = \frac{\nabla S}{|\nabla S|} \quad (3.18)$$

whereas the unit vector of the secondary reflected sub-ray, $\hat{\mathbf{R}}'_{ijkl,s} = R'_{sx}\hat{\mathbf{x}} + R'_{sy}\hat{\mathbf{y}} + R'_{sz}\hat{\mathbf{z}}$, can be calculated as:

$$\mathbf{R}'_{ijkl,s} = \begin{bmatrix} R'_{sx} \\ R'_{sy} \\ R'_{sz} \\ 1 \end{bmatrix}_{ijkl,s} = \begin{bmatrix} 2(R_{sx}N''_{sx} + R_{sy}N''_{sy} + R_{sz}N''_{sz})N''_{sx} - R_{sx} \\ 2(R_{sx}N''_{sx} + R_{sy}N''_{sy} + R_{sz}N''_{sz})N''_{sy} - R_{sy} \\ 2(R_{sx}N''_{sx} + R_{sy}N''_{sy} + R_{sz}N''_{sz})N''_{sz} - R_{sz} \\ 1 \end{bmatrix}_{ijkl,s} \quad (3.19)$$

Finally, the coordinate of the hitting point on target plane, $T_{ijkl,s} = (T_{sx}, T_{sy}, T_{sz})_{ijkl,s}$, can be determined by solving the line equation of the secondary reflected sub-ray and the surface equation of the target plane. The hitting point is expressed as:

$$\mathbf{T}_{ijkl,s} = \begin{bmatrix} T_{sx} \\ T_{sy} \\ T_{sz} \\ 1 \end{bmatrix}_{ijkl,s} = \begin{bmatrix} \frac{R'_{sx}}{R'_{sz}}(L - f_s - L_p - P_{sz}) + P_{sx} \\ \frac{R'_{sy}}{R'_{sz}}(L - f_s - L_p - P_{sz}) + P_{sy} \\ L - f_s \\ 1 \end{bmatrix}_{ijkl,s} \quad (3.20)$$

where L_p is the displacement of target plane from focal plane of secondary concentrator (positive means it is displaced towards the heliostat).

Each heliostat mirror of dimension $w \text{ cm} \times w \text{ cm}$ is represented by $n_{MR} \times n_{MR}$ reflective points, and a cone ray has n_{SD} sub-rays per aperture radius. The total number of sub-rays per cone ray can be estimated by $\pi \times n_{SD}^2$. Furthermore, the target plane of dimension $T_s \text{ cm} \times T_s \text{ cm}$ is represented by $n_{TR} \times n_{TR}$, which is fixed at 201 x 201 pixels. The solar concentration ratio (number of suns) of a particular pixel in the target plane is the ratio of how much irradiance the pixel receives over irradiance provided by one sun. If there are N sub-rays hitting a particular pixel, its solar concentration ratio can be calculated as:

$$C = \sum_{n=1}^{n=N} \frac{\text{area of reflective point (cm}^2\text{)}}{\text{area of target pixel (cm}^2\text{)}} \times \frac{\hat{L}(\alpha_s)}{\sum_{s=1}^{s=p} \hat{L}(\alpha_s)} \times \cos \theta_{ij} \quad (3.21)$$

where *area of reflective point* = $(w/n_{MR})^2$, *area of target pixel* = $(T_s/n_{TR})^2$, α_s is the angular displacement of sub-ray relative to centre of cone ray and θ_{ij} is the local incident angle relative to the corresponding ij -mirror.

3.3.3 Resolution

$$\text{Total pixels per mirror} = n_{MR} \times n_{MR}$$

$$\text{Total pixels per solar disc} = \pi \times n_{SD}^2$$

$$\text{Total pixels of target plane} = n_{TR} \times n_{TR}$$

$$\text{Mirror area} = w \times w$$

$$\text{Solar disc area} = \pi \times R_{SD}^2$$

$$\text{Target plane area} = T_s \times T_s$$

Resolution is redefined, courtesy of my supervisor, here as the number of pixels per unit area (unit of pixel per centimetre square or pixel/cm²).

The resolution of heliostat mirror:

$$r_{MR} = \left(\frac{n_{MR}}{w} \right)^2 \quad (3.22a)$$

The resolution of cone ray:

$$r_{SD} = \left(\frac{n_{SD}}{R_{SD}} \right)^2 \quad (3.22b)$$

The resolution of target plane:

$$r_{TR} = \left(\frac{n_{TR}}{T_s} \right)^2 \quad (3.22c)$$

where R_{SD} is the cross-sectional radius of cone ray projected on the target plane. For simplicity, it is calculated from a cone ray from the origin of heliostat, which leads to:

$$R_{SD} = (L + f_s + L_p) \tan \alpha_{aur} \quad (3.23)$$

The resolution of target plane is used as a reference to estimate the optimal resolutions for the mirror and cone ray. The resolution factor is expressed as:

$$k_1 = \frac{r_{MR}}{r_{TR}} \quad (3.24a)$$

$$k_2 = \frac{r_{SD}}{r_{TR}} \quad (3.24b)$$

CHAPTER 4

RESULTS AND DISCUSSION

4.1 Introduction

Figure 4.1 and Figure 4.2 show the 3D and 2D plot of the flux distribution profile produced by solar furnace using highest resolution ($r_{MR} = 3$, $r_{SD} = 7$) respectively. Maximum solar concentration ratio (C_{max}) is defined in the plot.

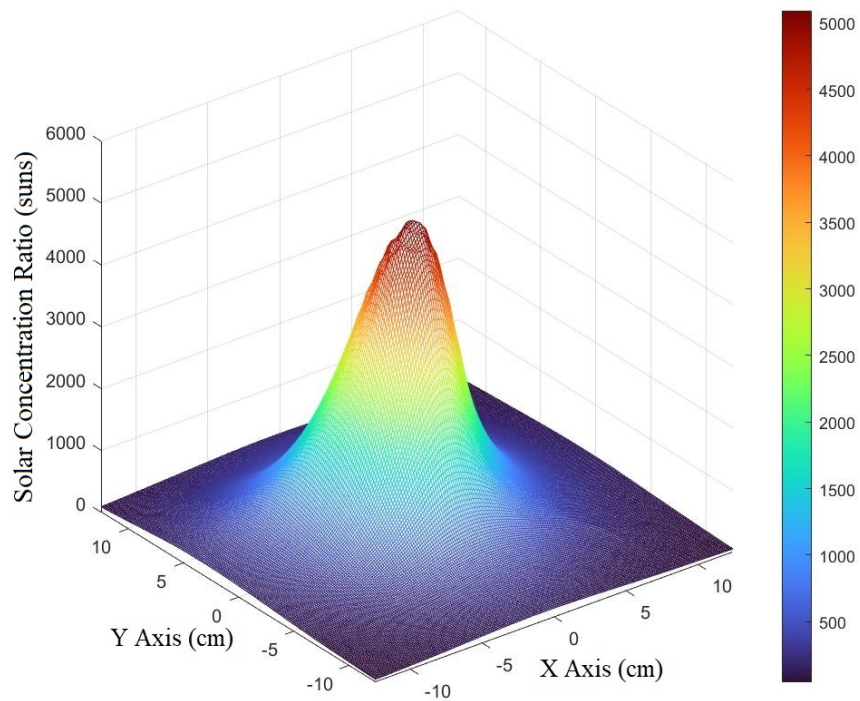


Figure 4.1: 3D Plot of Solar Flux Distribution.

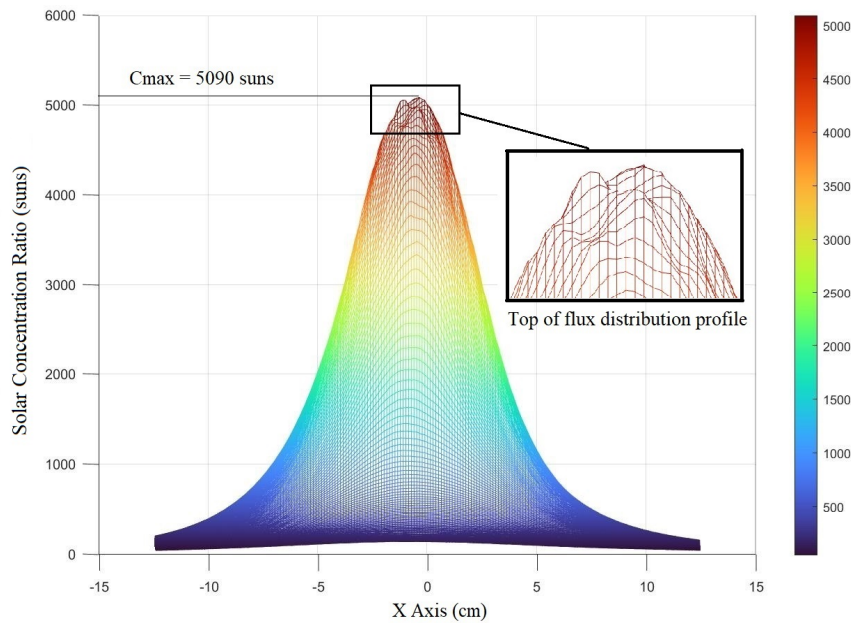


Figure 4.2: 2D Plot of Solar Flux Distribution.

4.2 Optimization

The mirror and cone ray resolutions affect the trade-off between result accuracy and simulation time. Highly accurate flux distribution map can be obtained by tracing large number of rays, but this will lead to impractically long simulation time. Hence, it is important to determine the optimal resolutions that produce a reasonably accurate result. The parameter that is used to judge the accuracy of the solar flux distribution map is the maximum solar concentration ratio (C_{max}), in which the deviation of maximum solar concentration can be interpreted as the “roughness” of the flux distribution profile. Logically, maximum solar concentration should approach a steady state or “true” value with increasing resolution or simulation time. The optimal resolution is defined such that maximum solar concentration is within 1 % deviation from the “true” value.

4.2.1 Importance of Optimization

The total number of rays traced can be estimated as:

$$N_{ray} = N_{mirror} \times n_{MR}^2 \times \pi \times n_{SD}^2 \quad (4.1)$$

The number of rays traced depends on n_{MR} and n_{SD} , which are determined by resolutions r_{MR} and r_{SD} . To plot to graph of computation time versus total number of rays traced, the simulation was repeated with various combinations of n_{MR} and n_{SD} . Figure 4.3 shows that the computation time (t) is linearly proportional to the number of rays traced (N_{ray}) by fulfilling the equation $t = 1.8235 \times 10^{-6} N_{ray}$. Naturally, the computation time and hence, the equation varies for different computers used.

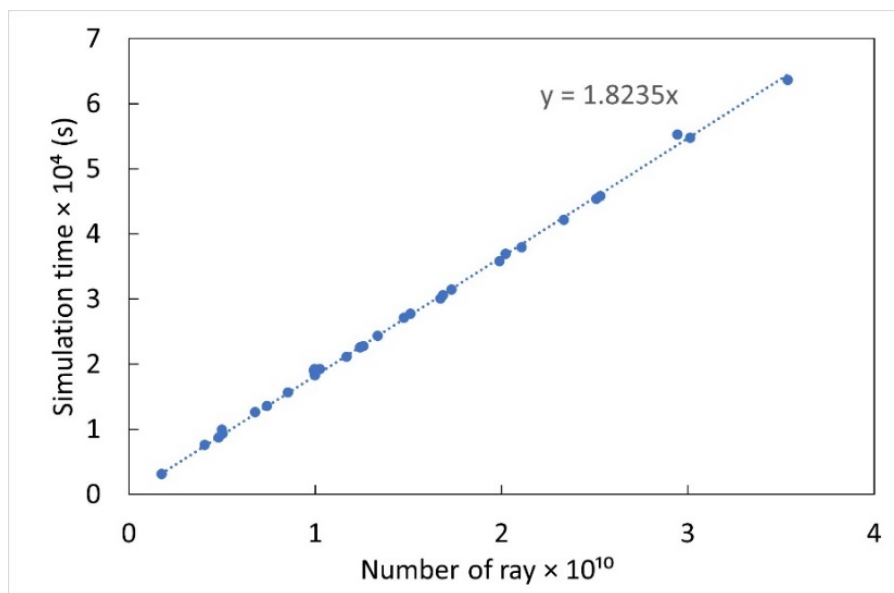


Figure 4.3: Graph of Computation Time Versus Total Number of Rays Traced.

As the accuracy of the flux distribution is dependent on number of rays traced, simulation data has been collected to investigate the deviation of maximum solar concentration with respect to simulation time. The deviation of maximum solar concentration is defined as the percentage error from the “true” value of maximum solar concentration, in which the number of rays to be traced for obtaining this “true” value is a generous 35 billion rays. Figure 4.4 shows the graph of deviation of maximum solar concentration versus simulation time.

Bear in mind the X-axis is logarithmic. From the graph, maximum solar concentration rapidly converges to the “true” value: just 100 seconds to achieve < 20 % deviation, 1000 seconds to achieve < 5 % deviation and 10000 seconds to achieve < 1 % deviation. However, diminishing returns are significant for longer simulation times, e.g., from 1000 seconds to 10000 seconds, which is ten times longer, only improves the deviation from 5 % to 1 %, which is a 4 % improvement.

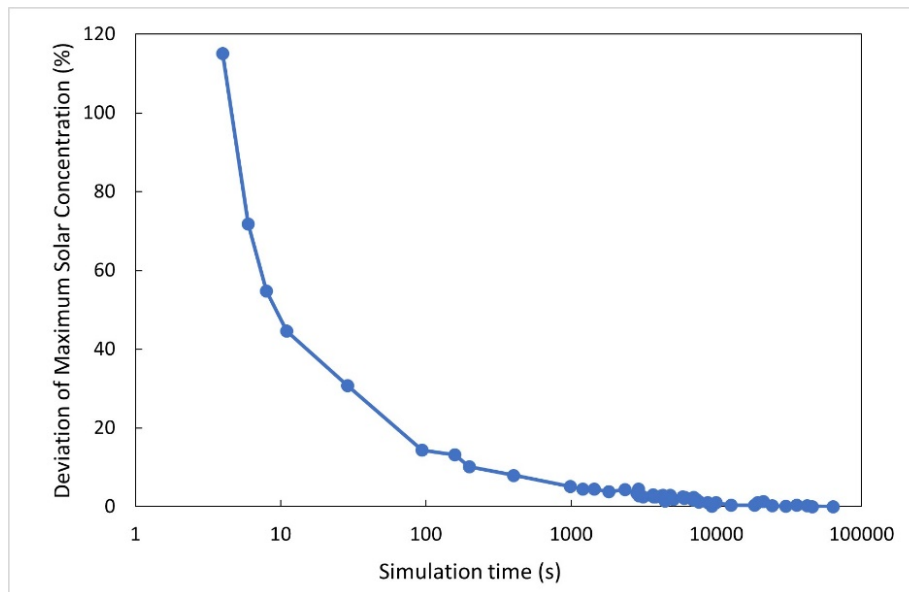


Figure 4.4: Graph of Deviation of Maximum Solar Concentration Versus Simulation Time.

4.2.2 Optimization Techniques

Maximum solar concentration (Figure 4.5 and Figure 4.6) and the top of flux distribution profile (Table 4.1 and Table 4.2) are plotted with respect to k_1 and k_2 to see the effect of resolution. Higher values of k_1 and k_2 correspond to higher mirror and solar disc resolution respectively.

From Figure 4.5, maximum solar concentration converges to a steady state value with increasing k_1 for a fixed k_2 . Interestingly, a similar thing occurs when k_1 and k_2 are switched (Figure 4.6). The resolutions that are around 1 % deviation from the steady state values are $k_1 = 46 \times 10^{-3}$ and $k_2 = 15 \times 10^{-3}$. These will be the optimal resolution values and henceforth be used for the rest of the report.

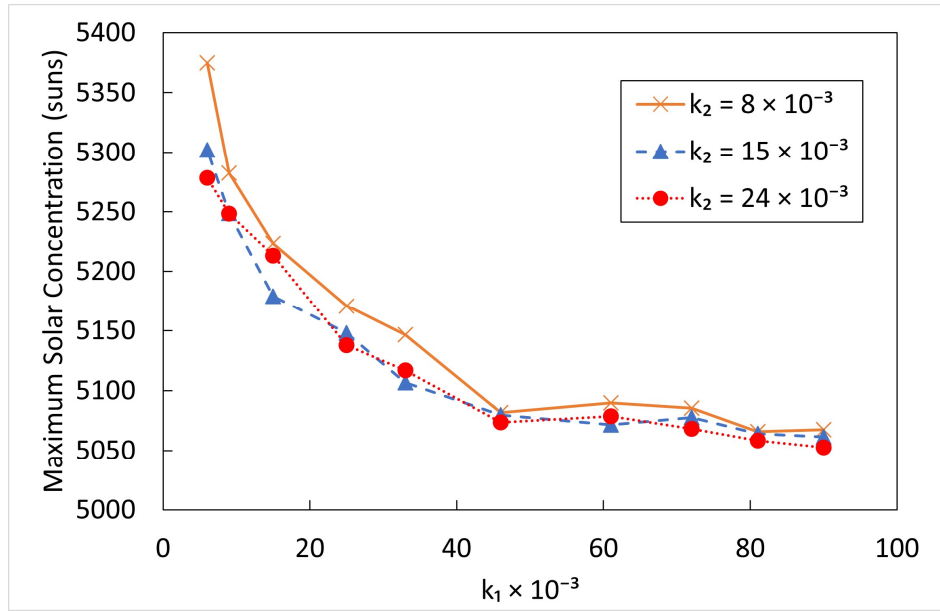


Figure 4.5: Graph of Maximum Solar Concentration Versus k_1 for Fixed k_2 .

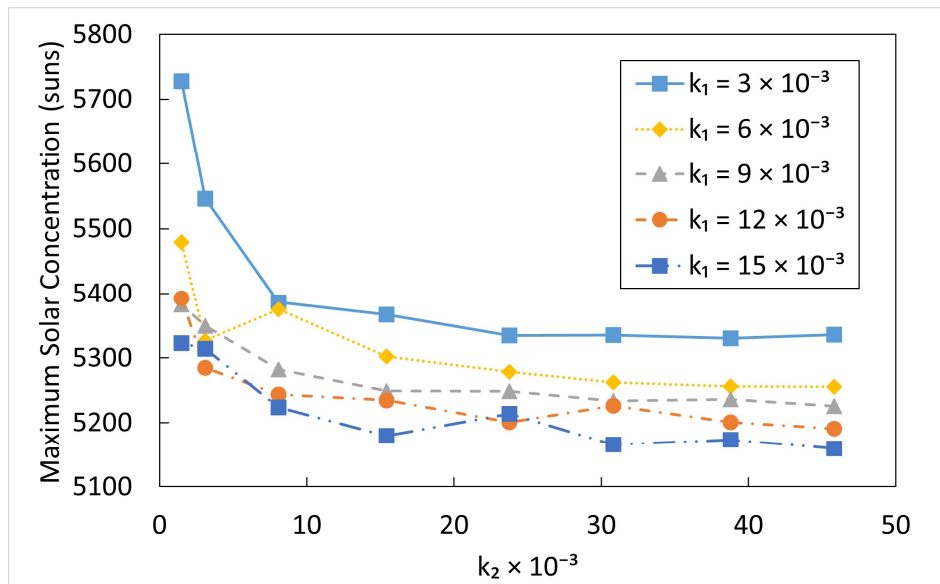


Figure 4.6: Graph of Maximum Solar Concentration Versus k_2 for Fixed k_1 .

Optimizing the resolution solely based on maximum solar concentration may not produce a sufficiently accurate flux distribution. Hence, for a more comprehensive study, careful observation of the flux distribution pattern becomes important. In Table 4.1 and Table 4.2, the tops of the flux distribution profiles are listed with respect to k_1 and k_2 . From the table, low resolutions produce jagged profiles. Low number of rays mean that each ray from the

heliostat mirror must carry a large solar concentration value, causing the sudden spikes. Increasing values of k_1 and k_2 show obvious improvement on the shape and smoothness of flux distribution, where the pattern matures, and sharp spikes gradually disappear.

Table 4.1: Top of Flux Distribution for Increasing k_1 for Fixed k_2 .

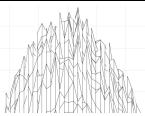
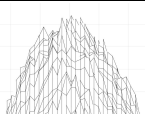
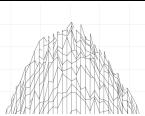
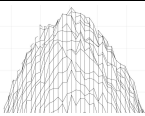
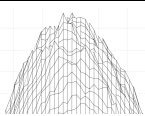
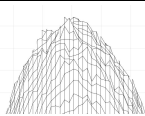
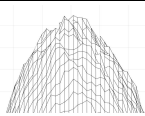
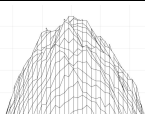
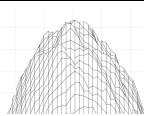
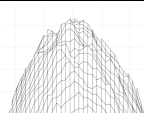
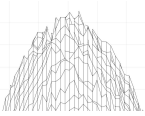
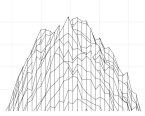
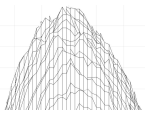
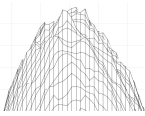
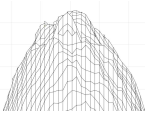
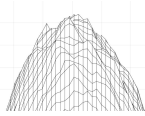
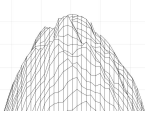
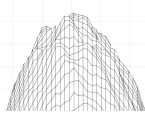
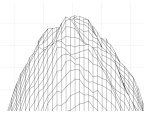
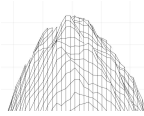
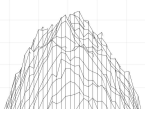
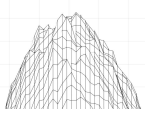
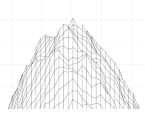
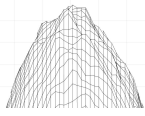
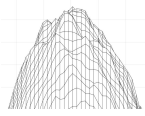
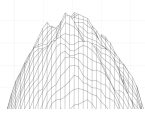
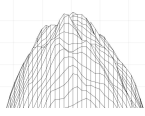
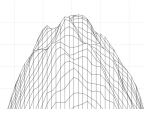
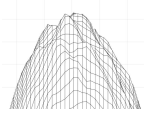
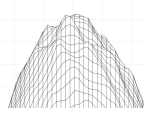
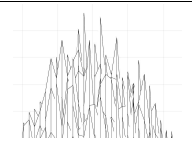
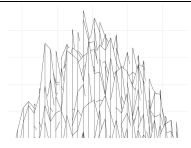
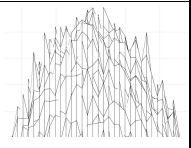
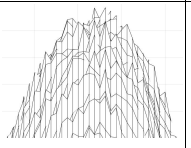
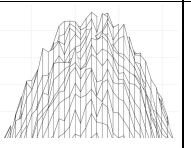
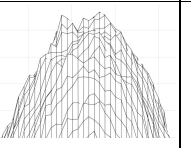
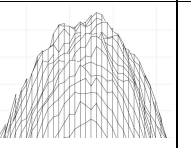
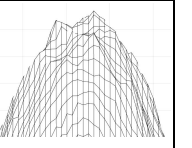
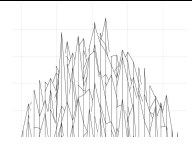
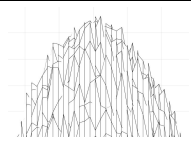
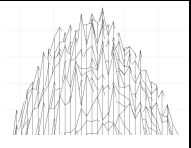
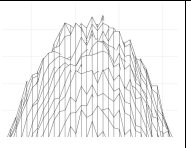
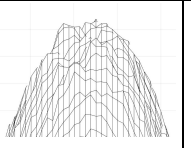
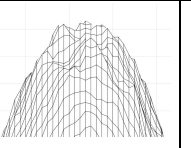
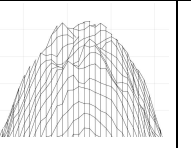
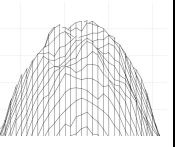
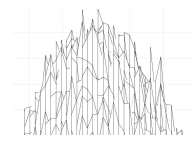
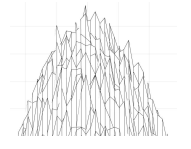
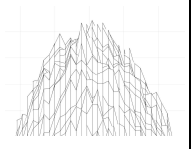
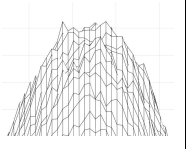
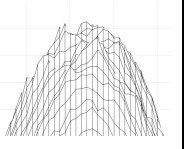
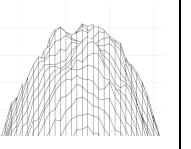
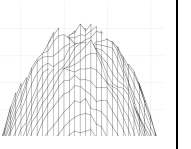
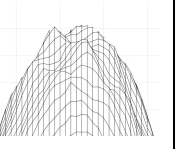
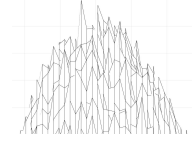
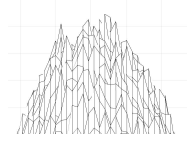
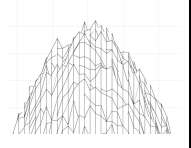
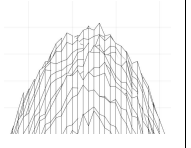
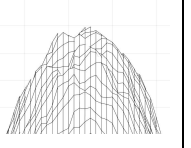
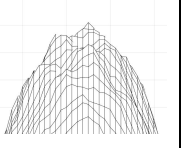
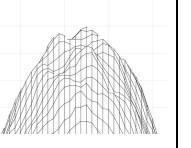
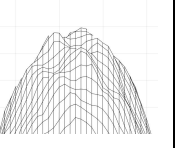
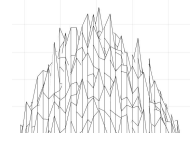
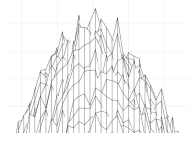
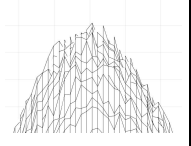
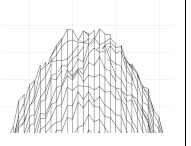
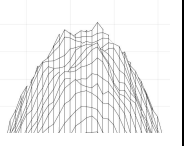
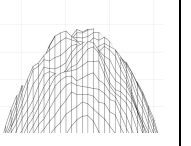
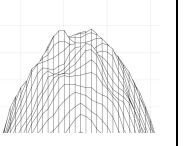
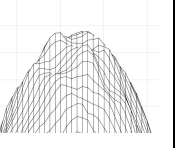
	$\Gamma_{MR}=0.4$ $k_1=6\times 10^{-3}$	$\Gamma_{MR}=0.6$ $k_1=9\times 10^{-3}$	$\Gamma_{MR}=1.0$ $k_1=15\times 10^{-3}$	$\Gamma_{MR}=1.6$ $k_1=25\times 10^{-3}$	$\Gamma_{MR}=2.1$ $k_1=33\times 10^{-3}$	$\Gamma_{MR}=2.9$ $k_1=46\times 10^{-3}$	$\Gamma_{MR}=3.9$ $k_1=61\times 10^{-3}$	$\Gamma_{MR}=4.6$ $k_1=72\times 10^{-3}$	$\Gamma_{MR}=5.2$ $k_1=81\times 10^{-3}$	$\Gamma_{MR}=5.8$ $k_1=90\times 10^{-3}$
$\Gamma_{SD}=0.5$ $k_2=8\times 10^{-3}$										
$\Gamma_{SD}=1.0$ $k_2=15\times 10^{-3}$										
$\Gamma_{SD}=1.5$ $k_2=24\times 10^{-3}$										

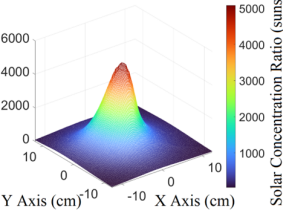
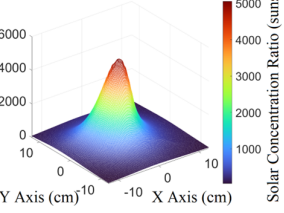
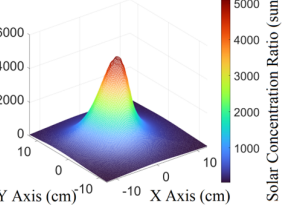
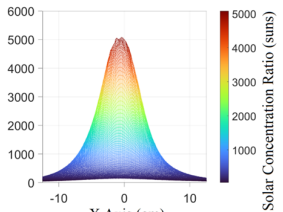
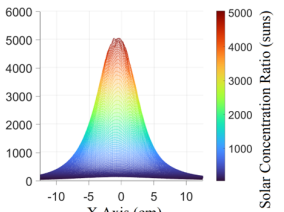
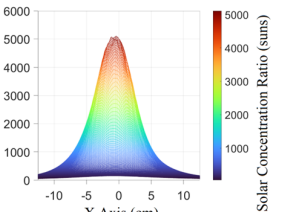
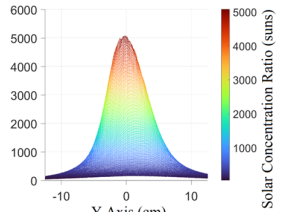
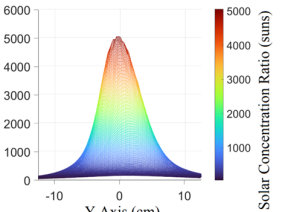
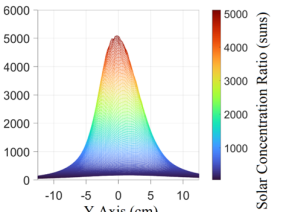
Table 4.2: Top of Flux Distribution for Increasing k_2 for Fixed k_1 .

	$r_{SD}=0.1$ $k_2=1 \times 10^{-3}$	$r_{SD}=0.2$ $k_2=3 \times 10^{-3}$	$r_{SD}=0.5$ $k_2=8 \times 10^{-3}$	$r_{SD}=1.0$ $k_2=15 \times 10^{-3}$	$r_{SD}=1.5$ $k_2=24 \times 10^{-3}$	$r_{SD}=2.0$ $k_2=31 \times 10^{-3}$	$r_{SD}=2.5$ $k_2=39 \times 10^{-3}$	$r_{SD}=3.0$ $k_2=46 \times 10^{-3}$
$r_{MR}=0.2$ $k_1=3 \times 10^{-3}$								
$r_{MR}=0.4$ $k_1=6 \times 10^{-3}$								
$r_{MR}=0.6$ $k_1=9 \times 10^{-3}$								
$r_{MR}=0.8$ $k_1=12 \times 10^{-3}$								
$r_{MR}=1.0$ $k_1=15 \times 10^{-3}$								

4.2.3 Comparison with Highest Resolution

To show that the k_1 and k_2 selected previously are optimal, a comparison with the highest resolution available simulation result is performed (Table 4.3). As there are two resolutions, k_1 and k_2 , it is difficult to determine which is the highest resolution result. Here, four candidates are proposed: highest k_1 , highest k_2 , largest number of rays (or longest simulation time), and lowest maximum solar concentration. For the optimal k_1 and k_2 selected previously, the deviation of maximum solar concentration is $< 1 \%$. Furthermore, a mature flux distribution pattern can already be observed, where there are not many differences compared to highest resolution profiles.

Table 4.3: Comparison between Optimal Resolution, Highest k_1 and Lowest Maximum Solar Concentration, and Highest k_2 and Largest Number of Rays.

	$k_1 = 46 \times 10^{-3}$ $k_2 = 15 \times 10^{-3}$ (Optimal resolution)	$k_1 = 90 \times 10^{-3}$ $k_2 = 24 \times 10^{-3}$ (Highest k_1) (Lowest C_{max})	$k_1 = 47 \times 10^{-3}$ $k_2 = 112 \times 10^{-3}$ (Highest k_2) (Most rays)
3D			
X Axis			
Y Axis			
C_{max}	5080 suns	5053 suns	5108 suns

4.3 Verification of Simulation Results

Simulation results can be verified by judging how well it matches with the experimental results. Lim and Li (2009) provided an image of a steel plate melted by a solar furnace (Figure 4.7), in which the specifications of the solar furnace are given. The simulation specifications are listed in Table 4.4 (CSR and Slope Error are assumed to be 0.01 and 0.001 respectively) and the resulting solar flux distribution profile is shown in Figure 4.8.



Figure 4.7: Steel Plate Melted by a Solar Furnace (Lim and Li, 2009).

Table 4.4: Specifications for the Simulation of Solar Furnace Described in an Article by Lim and Li.

Parameter	Value
Target distance	2400 cm
Target size	20 cm
Mirror gap	1 cm
Mirror size	45 cm
Mirror focal length	2400 cm
Target position	-2 cm
Incident angle	28°
Spinning angle	0
Operational angle	36°
Number of row and column	11
Secondary concentrator diameter	46 cm
Secondary concentrator focal length	23 cm
Heliostat focal length	2400 cm
CSR	0.01
Slope error	0.001
Motor	M+N-2 motor
Secondary concentrator type	Spherical

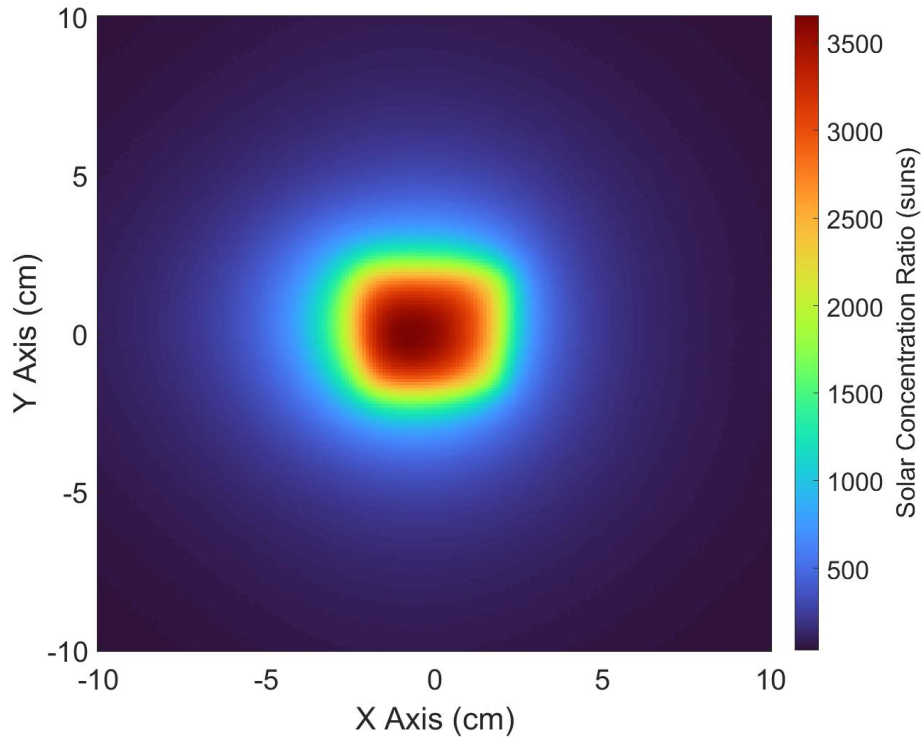


Figure 4.8: Top View of Solar Flux Distribution of Steel Plate.

4.3.1 Temperature Distribution Map

To obtain the temperature distribution map of the target, the solar concentration ratios of the target pixels are converted into temperature as described by Stefan-Boltzmann law:

$$I = e\sigma T^4 \quad (4.2)$$

where I is the intensity on the target pixel and $I = \text{intensity of one sun} \times \text{solar concentration ratio}$, e is the emissivity of the target material, σ is Stefan-Boltzmann constant ($\sigma = 5.67 \times 10^8 \text{ Wm}^{-2}\text{K}^{-4}$) and T is the absolute temperature. The values provided or assumed: $\text{intensity of one sun} = 800 \text{ Wm}^{-2}$ and $e_{\text{steel}} = 0.96$. Figure 4.9 shows the temperature distribution map of the steel plate.

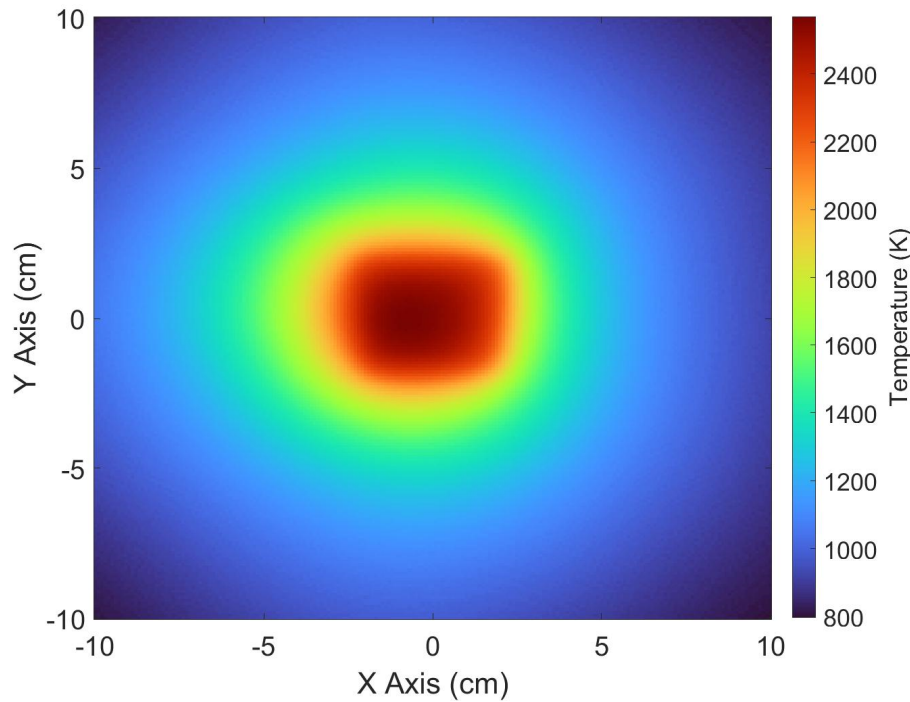


Figure 4.9: Temperature Distribution Map of Steel Plate.

4.3.2 Comparison between Experimental and Simulation Results

The accuracy of the results can be judged based on the similarity of the size and shape of the melting spot. Figure 4.10 shows the photo of the melted steel plate and the temperature distribution map with an additional black contour of the melting point of steel of 1800 K. The horizontal lengths of the melting boundaries are also extrapolated from the scales given using a measuring software.

In terms of size, the horizontal length of the melting boundary of the ideal simulated result is larger by 44.79 %. The smaller melting spot of the real steel plate may be attributed to heat loss through radiation of heat to the environment and conduction of heat to the rest of the steel plate out of melting spot. Furthermore, the steel plate may not be melted for long enough to obtain the full size of the melting spot. This is evidenced by the steel plate being gradually melted instead of being completely melted through. Lastly, the various assumptions made to obtain the temperature distribution map may not be accurate. As an example, the constant irradiance of 800 Wm^{-2} may be unrealistic.

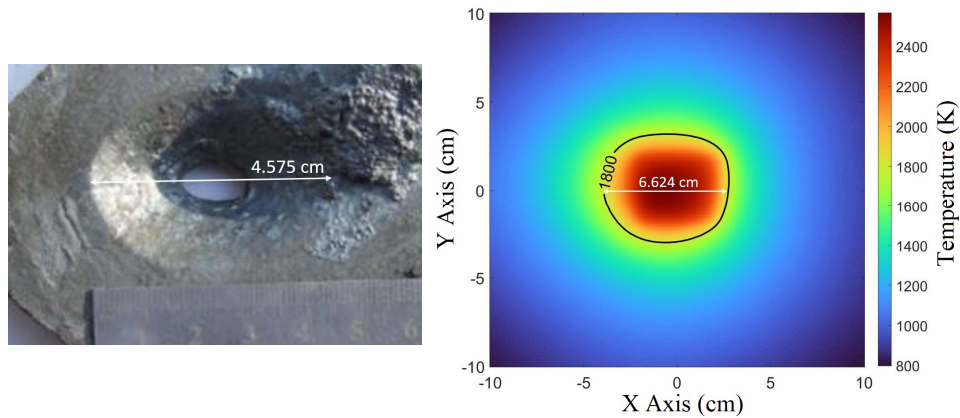


Fig. 4.10: Comparison of Melted Steel Plate (Lim and Li, 2009) (left) and Temperature Distribution Map (right).

In terms of shape, the resemblance between both results is high. As illustrated in Figure 4.11, it is apparent when the melting contour of 1800 K in white is overlaid on top of the steel plate. The contour is scaled down to compensate for the size difference and compressed vertically to compensate for camera tilt.



Fig. 4.11: Melting Contour Overlaid on Top of the Steel Plate (Lim and Li, 2009).

4.4 Solar Pyrolysis of Mixed Plastic Waste

Pyrolysis is the thermal decomposition of materials at elevated temperatures in the absence of oxygen. It is a common technique used to convert plastic waste into energy, in the form of solid, liquid, and gaseous fuels (Miandad, et al., 2019). The best temperature for the pyrolysis of such plastic waste in terms of conversion and product quality has been determined to be 500 °C or 773 K (López, et al., 2011).

4.4.1 Feasibility of Solar Furnace

Various factors affect the flux distribution and the corresponding temperature map produced by the solar furnace. In terms of the flux distribution, the sun path varies throughout the year and changes the incident and rotation angle of the heliostat. Courtesy of my supervisor, Figure 4.12 and Figure 4.13 shows the variation of incident and rotation angle for the heliostat operating in Yinchuan, Ningxia, China (38.47° N, 106.27° E) respectively. In terms of the temperature map, the solar irradiance affects the conversion of solar concentration ratio to temperature. Solar Irradiance Data used in Table 4.5 was retrieved from Solcast (Solcast, 2023).

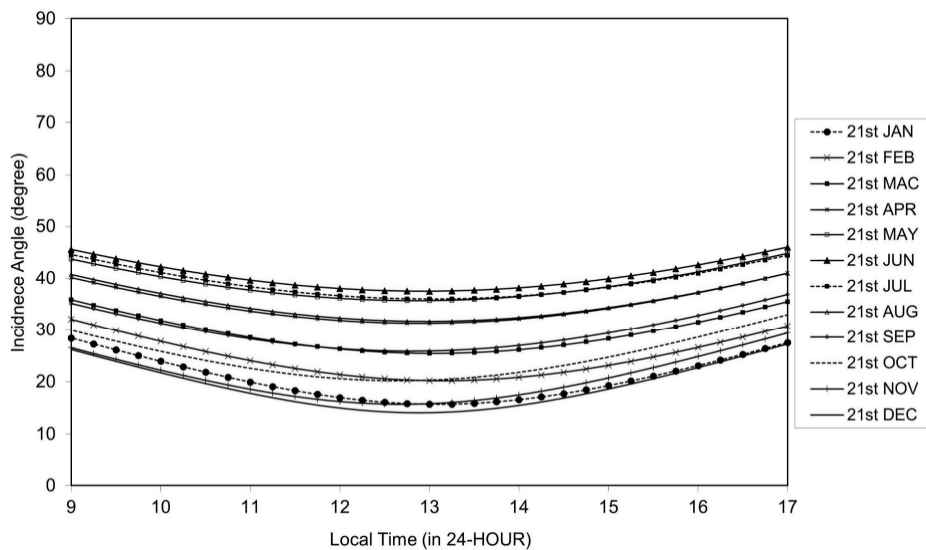


Fig. 4.12: Variation of Incidence Angle of Heliostat Operating at Yinchuan, Ningxia, China.

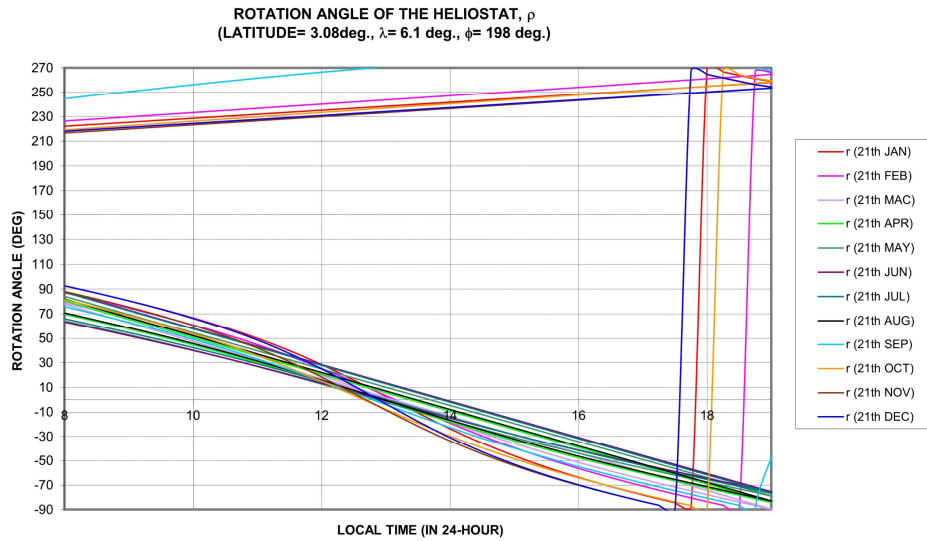


Fig. 4.13: Variation of Rotation Angle of Heliostat Operating at Yinchuan, Ningxia, China.

To show that the solar furnace can achieve the temperatures that are required for solar pyrolysis of mixed plastic waste, the flux distribution and the corresponding temperature map of the solar furnace operating in Yinchuan has been simulated for 21 June 2021 (summer solstice) (Table 4.5a), 22 December 2022 (winter solstice) (Table 4.5b) and 20 March 2022 (vernal equinox) (Table 4.5c). Although the temperature map may be idealistic, e.g., assuming a black body and no heat loss, for reasonable solar irradiance, the solar furnace easily achieves plastic pyrolysis temperature of 773 K.

Table 4.5a: Flux Distribution, Temperature Map and Solar Irradiance Data at Yinchuan, Ningxia, China on 21 June 2021 (Summer Solstice).

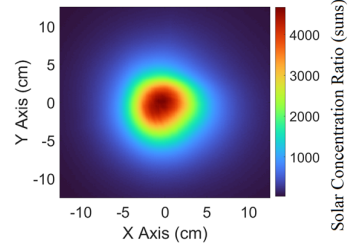
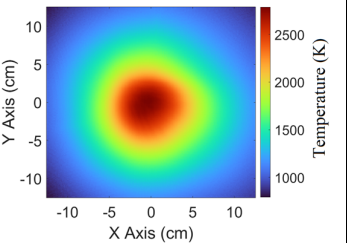
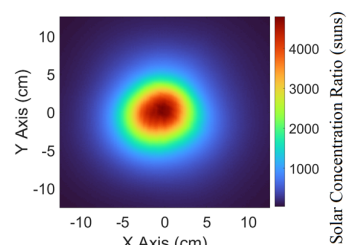
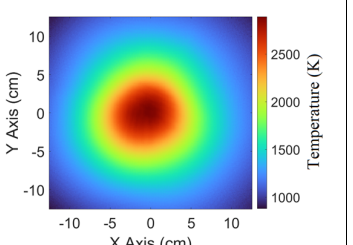
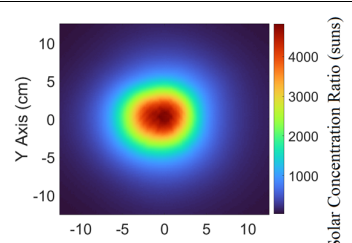
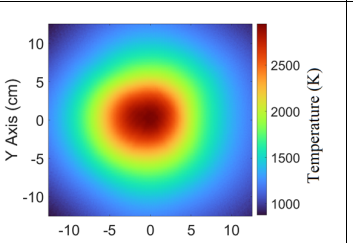
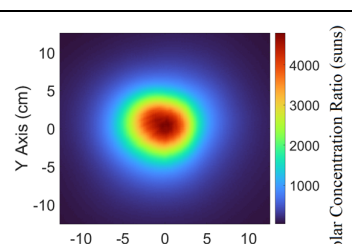
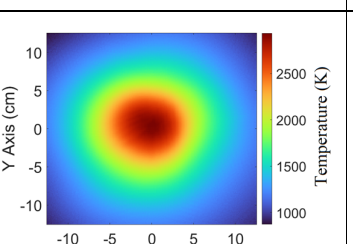
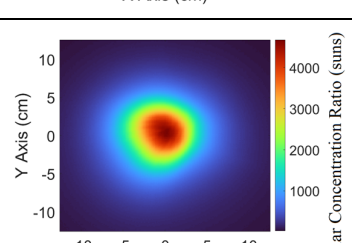
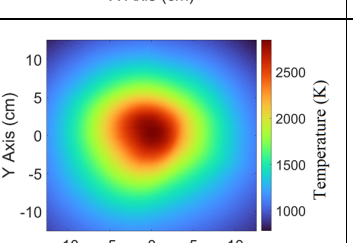
Time	Flux distribution	Temperature map	Irradiance (W/m ²)
9am			733
11am			827
1pm			888
3pm			876
5pm			798

Table 4.5b: Flux Distribution, Temperature Map and Solar Irradiance Data at Yinchuan, Ningxia, China on 22 December 2022 (Winter Solstice).

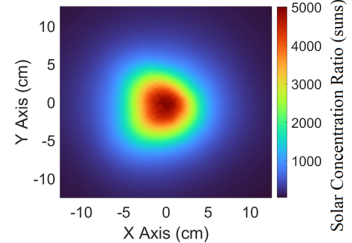
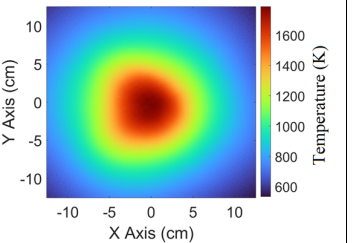
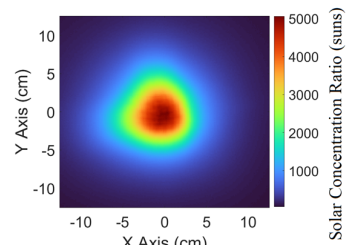
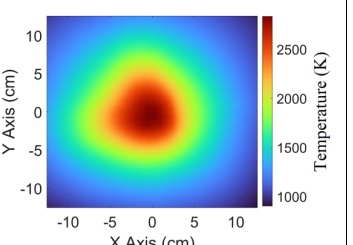
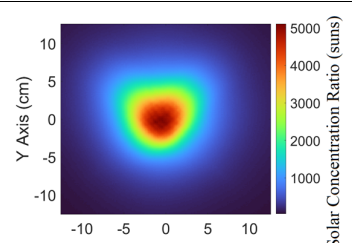
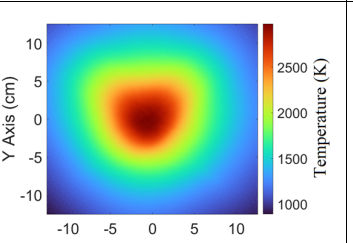
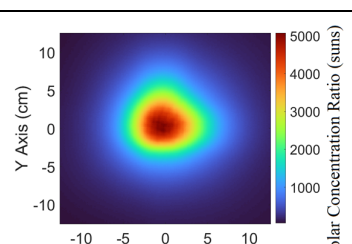
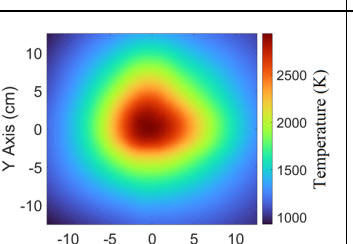
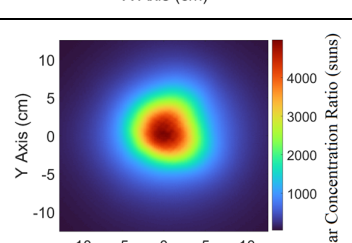
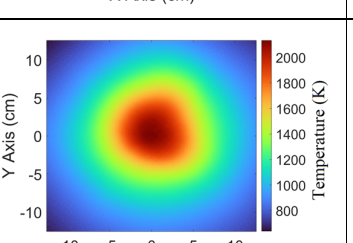
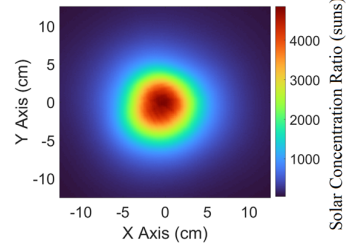
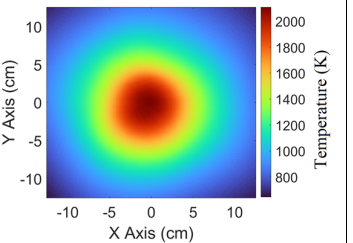
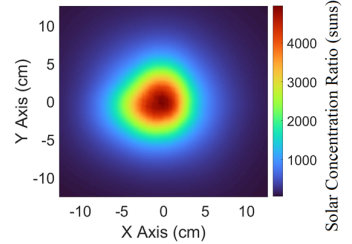
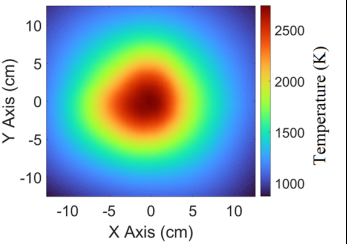
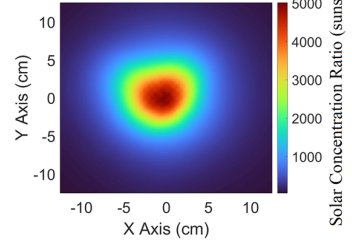
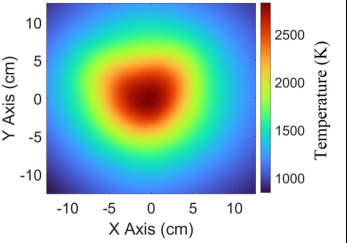
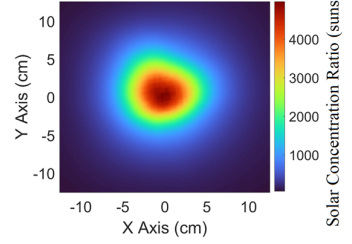
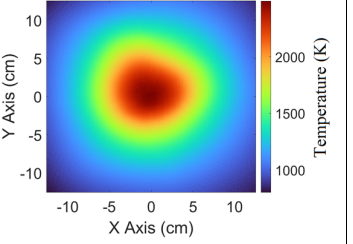
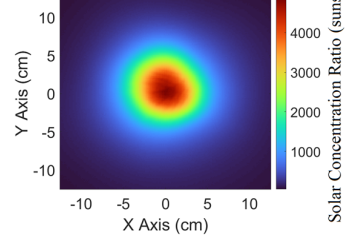
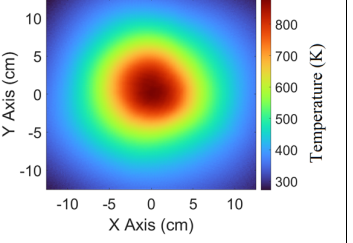
Time	Flux distribution	Temperature map	Irradiance (W/m ²)
9am			116
11am			724
1pm			868
3pm			832
5pm			236

Table 4.5c: Flux Distribution, Temperature Map and Solar Irradiance Data at Yinchuan, Ningxia, China on 20 March 2022 (Vernal Equinox).

Time	Flux distribution	Temperature map	Irradiance (W/m ²)
9am			231
11am			646
1pm			723
3pm			439
5pm			7

CHAPTER 5

CONCLUSIONS AND RECOMMENDATIONS

5.1 Conclusions

A simulation software has been used to study the solar flux distribution of the hot spot produced by the new solar furnace system consisting of a heliostat and secondary concentrator. The details of the modelling and ray-tracing algorithm have been presented. For computational simulations, the trade-off between result accuracy and simulation time is important. Hence, optimal resolutions taking into account both the value and geometrical profile of simulated results have been determined, where optimal mirror resolution factor $k_1 = 46 \times 10^{-3}$ and optimal cone ray resolution factor $k_2 = 15 \times 10^{-3}$. For verification of the simulation algorithm, a comparison of the simulated and experimental melting spot of a steel plate has been made. To show that the solar furnace is feasible for application in solar pyrolysis of mixed plastic waste, a case study of a solar furnace operating at Yinchuan, Ningxia, China during solstices and equinoxes has been simulated.

5.2 Recommendations for Future Work

The following are recommended for further research based on the flaws and limitations of the study:

- (i) Determine whether the optimal resolutions found are still optimal when the simulation specifications (e.g., target distance, mirror size, and target size) are changed.
- (ii) Use a more realistic approach to determine the feasibility of solar furnace such as considering reflection losses of mirror, emissivity of target material and solar irradiance across a period of time.

REFERENCES

- Buie, D., Monger, A.G. and Dey, C.J., 2003. Sunshape distributions for terrestrial solar simulations. *Solar Energy*, [e-journal] 74(2), pp.113-122. [https://doi.org/10.1016/S0038-092X\(03\)00125-7](https://doi.org/10.1016/S0038-092X(03)00125-7).
- Chen, Y.T., Chong, K.K., Bligh, T.P., Chen, L.C., Yunus, J., Kannan, K.S., Lim, B.H., Lim, C.S., Alias, M.A., Bidin, N., Aliman, O., Salehan, S., S.A.H., Shk. Abd. Rezan, Tam, C.M. and Tan, K.K., 2001. Non-Imaging, Focusing Heliostat. *Solar Energy*, [e-journal] 71(3), pp.155-164. [https://doi.org/10.1016/S0038-092X\(01\)00041-X](https://doi.org/10.1016/S0038-092X(01)00041-X).
- Chong, K.K., 2010. Optical analysis for simplified astigmatic correction of non-imaging focusing heliostat. *Solar Energy*, [e-journal] 84(8), pp.1356-1365. <https://doi.org/10.1016/j.solener.2010.04.013>.
- Hisada, T., Mii, H., Noguchi, C., Noguchi, T., Hukuo, N. and Mizuno, M., 1957. Concentration of the solar radiation in a solar furnace. *Solar Energy*, [e-journal] 1(4), pp.14-16. [https://doi.org/10.1016/0038-092X\(57\)90166-4](https://doi.org/10.1016/0038-092X(57)90166-4).
- Kevane, C.J., 1957. Construction and operation of the Arizona State College solar furnace. *Solar Energy*, [e-journal] 1(2-3), pp.99-101. [https://doi.org/10.1016/0038-092X\(57\)90129-9](https://doi.org/10.1016/0038-092X(57)90129-9).
- Lee, H., Chai, K., Kim, J., Lee, S., Yoon, H., Yu, C. and Kang, Y., 2014. Optical performance evaluation of a solar furnace by measuring the highly concentrated solar flux. *Energy*, [e-journal] 66, pp.63-69. <https://doi.org/10.1016/j.energy.2013.04.081>.
- Li, B., Oliveira, F.J., Rodriguez, J.A., Fernandes, J.O. and Bicudo, F., 2015. Numerical and experimental study on improving temperature uniformity of solar furnaces for materials processing. *Solar Energy*, [e-journal] 115, pp.95-108. <https://doi.org/10.1016/j.solener.2015.02.023>.
- Lim, C.S. and Li, L., 2009. Flux distribution of solar furnace using non-imaging focusing heliostat. *Solar Energy*, [e-journal] 83(8), pp.1200-1210. <https://doi.org/10.1016/j.solener.2009.02.002>.
- López, A., de Marco, I., Caballero, B.M., Laresgoiti, M.F. and Adrados, A., 2011. Influence of time and temperature on pyrolysis of plastic wastes in a semi-batch reactor. *Chemical Engineering Journal*, [e-journal] 173(1), pp.62-71. <https://doi.org/10.1016/j.cej.2011.07.037>.
- Lu, C.-H. and Sung, C.-K., 2013. Skew ray tracing and sensitivity analysis of hyperboloid optical boundary surfaces. *Optik*, [e-journal] 124(12), pp.1159-1169. <https://doi.org/10.1016/j.ijleo.2012.03.014>.

Miandad, R., Rehan, M., Barakat, M.A., Aburiazaiza, A.S., Khan, H., Ismail, I.M.I., Dhavamani, J., Gardy, J., Hassanpour, A. and Nizami, A.-S., 2019. Catalytic Pyrolysis of Plastic Waste: Moving Toward Pyrolysis Based Biorefineries. *Frontiers in Energy Research*, [e-journal] 7. <https://doi.org/10.3389/fenrg.2019.00027>.

Oliveira, F.A.C., Fernandes, J.C., Rodríguez, J., Cañadas, I., Galindo, J. and Rosa, L.G., 2016. Temperature uniformity improvement in a solar furnace by indirect heating. *Solar Energy*, [e-journal] 140, pp.141-150. <https://doi.org/10.1016/j.solener.2016.11.004>.

Solcast, 2023. Solar Irradiance Data. <https://solcast.com>.

Trombe, F., 1957. Solar furnaces and their applications. *Solar Energy*, [e-journal] 1(2-3), pp.9-15. [https://doi.org/10.1016/0038-092X\(57\)90115-9](https://doi.org/10.1016/0038-092X(57)90115-9).

Trombe, F. and Le Phat Vinh, A., 1973. Thousand kW solar furnace, built by the National Center of Scientific Research, in Odeillo (France). *Solar Energy*, [e-journal] 15(1), pp.57-61. [https://doi.org/10.1016/0038-092X\(73\)90006-6](https://doi.org/10.1016/0038-092X(73)90006-6).

Wong, C.-W., Chong, K.-K. and Tan, M.-H., 2015. Performance optimization of dense-array concentrator photovoltaic system considering effects of circumsolar radiation and slope error. *Optics Express*, [e-journal] 23(15), pp.A841-A857. <https://doi.org/10.1364/OE.23.00A841>.